Numerical Simulations of Spatial Distributions and Diurnal Variations of Low-Level Jets in China during Early Summer

YU DU AND QINGHONG ZHANG

Laboratory for Climate and Ocean-Atmosphere Studies, Department of Atmospheric and Oceanic Sciences, School of Physics, Peking University, Beijing, China

YI-LENG CHEN

Department of Meteorology, School of Ocean and Earth Science and Technology, University of Hawai'i at Mānoa, Honolulu, Hawaii

YANGYANG ZHAO

Laboratory for Climate and Ocean-Atmosphere Studies, Department of Atmospheric and Oceanic Sciences, School of Physics, Peking University, Beijing, China

XU WANG

Weather Modification Office of Xingjiang Uygur Autonomous Region of China, Urumqi, China

(Manuscript received 19 September 2013, in final form 24 January 2014)

ABSTRACT

The detailed spatial distributions and diurnal variations of low-level jets (LLJs) during early summer (May–July) in China are documented using 2006–11 hourly model data from the Weather Research and Forecasting (WRF) Model with a 9-km horizontal resolution. It was found that LLJs frequently occur in the following regions of China: the Tarim basin, northeastern China, the Tibetan Plateau (TP), and southern China. The LLJs over China are classified into two types: boundary layer jets (BLJs, below 1 km) and synoptic-system-related LLJs (SLLJs, within 1–4 km). The LLJs in the Tarim basin and the TP are mainly BLJs. The SLLJs over southern China and northeastern China are associated with the mei-yu front and northeast cold vortex (NECV), respectively.

The BLJs in all regions show pronounced diurnal variations with maximum occurrences at nighttime or in the early morning, whereas diurnal variations of SLLJs vary, depending on the location. From the analysis of model data, the diurnal variation of BLJs is mainly caused by inertial oscillation at nighttime and vertical mixing in the boundary layer during daytime. Over northeastern China, SLLJ occurrences show little diurnal variation. Over southern China, two diurnal modes of SLLJs, propagation and stationary, exist and have seasonal variations, which is generally consistent with diurnal variations of precipitation.

1. Introduction

Low-level jets (LLJs) occur over many different parts of the world including North America (e.g., Bonner 1968; Whiteman et al. 1997), South America (e.g., Marengo et al. 2004; Vera et al. 2006), Africa (e.g., Todd et al. 2008), and Asia (e.g., Chen et al. 2005; Du et al. 2012). Owing to their close relationship with precipitation, there is broad interest in LLJs. Stensrud (1996) summarized regions of frequent LLJ occurrences around the globe based on previous literature. He concluded that LLJs prefer to occur next to a large mountain range or where land–sea temperature gradients exist. Using global downscaled reanalysis with a 40-km resolution, Rife et al. (2010) documented the quantitative global distribution of nocturnal LLJs (NLLJs) with an index of NLLJ activity based upon the temporal variations of the vertical wind profiles. They identified NLLJs in several new regions, including the Tarim basin in northwestern China,

Corresponding author address: Qinghong Zhang, Department of Atmospheric and Oceanic Sciences, School of Physics, Peking University, 209 Chengfu Road, Beijing 100871, China.
E-mail: qzhang@pku.edu.cn

DOI: 10.1175/JCLI-D-13-00571.1

Ethiopia in eastern Africa, and Namibia and Angola in southwest Africa. The distribution and characteristics of LLJs over the U.S. Great Plains have been well documented in previous studies (e.g., Bonner 1968; Blackadar 1957; Parish and Oolman 2010).

Most studies of LLJs in China focus on the relationship between LLJs and heavy rainfall using the case study approach, especially over southeastern China during the mei-yu season (e.g., Tao and Chen 1987; Chou et al. 1990; Zhang et al. 2000). Du et al. (2012) developed statistical characteristics of LLJs in Shanghai, a city in southern China, from wind profiler radar data. However, the overall horizontal and vertical distributions of LLJs over China are not well documented due to limitations of observational data compared to the U.S. Great Plains. Liu et al. (2012) and Wang et al. (2013) used the National Centers for Environmental Prediction (NCEP) Final (FNL) operational global analysis data with $1° \times 1°$ grids at 6-h intervals and 26 pressure levels to analyze the LLJs over southeastern China. Liu et al. (2012) found that these LLJs in the summer are closely related to topography and precipitation. Wang et al. (2013) suggested that these LLJs occur frequently in spring and summer with a maximum occurrence at night and are closely related to precipitation. Due to limitations in the temporal and spatial resolutions of FNL and global reanalysis, we will describe the occurrences, vertical structure, and horizontal distributions of LLJs in China during the early summer season in detail using model output data from long-term high-resolution numerical simulations.

The LLJs during the early summer over East Asia can be classified into two types according to their formation mechanisms and characteristics: 1) boundary layer jets (BLJs), which occur in the planetary boundary layer with significant vertical shear of horizontal wind and diurnal variation (Pham et al. 2008; Rife et al. 2010; Du et al. 2012); and 2) synoptic-system-related low-level jets (SLLJs), which occur in the 900- to 600-hPa layer and are usually related to synoptic-scale weather systems (Chen et al. 1994; Chen and Chen 1995; Du et al. 2012). Using wind profiler radar data, Du et al. (2012) observed the occurrence of both BLJs and SLLJs in Shanghai; however, a thorough description of the occurrences of BLJs and SLLJs in different locations in China is needed. In this study, we will document in detail the spatial distributions of BLJs and SLLJs in China using a high-resolution mesoscale model. The model is also used as a diagnostic tool to better understand the physical processes that are essential for the occurrences of LLJs.

The diurnal variations of BLJs with a maximum strength and occurrence at night or in the early morning are an important feature for BLJs in different parts of the world (e.g., Bonner 1968; Douglas et al. 1998; Pham et al. 2008). Inertial oscillation (Blackadar 1957; Van de Wiel et al. 2010) and baroclinicity over a sloping terrain or coastal areas (Holton 1967) are considered the two main causes for the occurrence of nocturnal BLJs. BLJs exhibit veering of winds similar to what we expect from inertial oscillations, with a clear clockwise rotation of the winds with time (Song et al. 2005; Du et al. 2012). From observations of low-level winds at Puerto Peñasco, Douglas et al. (1998) show that the diurnal variation of low-level winds is limited to the lowest 1800 m above the ground level, and its amplitude decreases with increasing height. Du et al. (2012) found that the diurnal variations of SLLJs are not as evident as for BLJs in Shanghai because the SLLJs are related to the synoptic weather systems, which exhibit little diurnal variations. Understanding the mechanisms of diurnal variations of BLJs and SLLJs in different parts of China is another interesting and important goal of this study. The physical processes responsible for these variations will be examined.

In this paper, the hourly model outputs with a 9-km horizontal resolution nonhydrostatic mesoscale Weather Research and Forecasting (WRF) Model (hereinafter "WRF") during the early summer (May–July) from 2006 to 2011 are used to compile the distribution and diurnal variations of LLJs in China. In section 2, we present a detailed procedure for our numerical simulations and the statistical methods used. Validation of the model dataset using the sounding data and wind profiler data at five different stations is given in section 3. In section 4, we present the spatial distributions of the occurrences of BLJs and SLLJs in China. In section 5, we describe the diurnal variations of BLJs and SLLJs in different regions and briefly discuss the mechanisms. The final section summarizes our results.

2. Model and methodology

a. Data and model

The Advanced Research Weather Research and Forecasting (WRF-ARW) Model (version 3.3.1, hereinafter "WRF-ARW") with a 9-km horizontal resolution and 40 eta layers[1] in the vertical direction is employed in this study. The simulation covers all of China (Fig. 1) during the early summer (May–July) from 2006 to 2011. Each

[1] η layer levels: 1.0000, 0.9974, 0.9940, 0.9905, 0.9850, 0.9800, 0.9700, 0.9600, 0.9450, 0.9300, 0.9100, 0.8900, 0.8650, 0.8400, 0.8100, 0.7800, 0.7500, 0.7100, 0.6800, 0.6450, 0.6100, 0.5700, 0.5300, 0.4900, 0.4500, 0.4100, 0.3700, 0.3300, 0.2900, 0.2500, 0.2100, 0.1750, 0.1450, 0.1150, 0.0900, 0.0650, 0.0450, 0.0250, 0.0100, 0.0000.

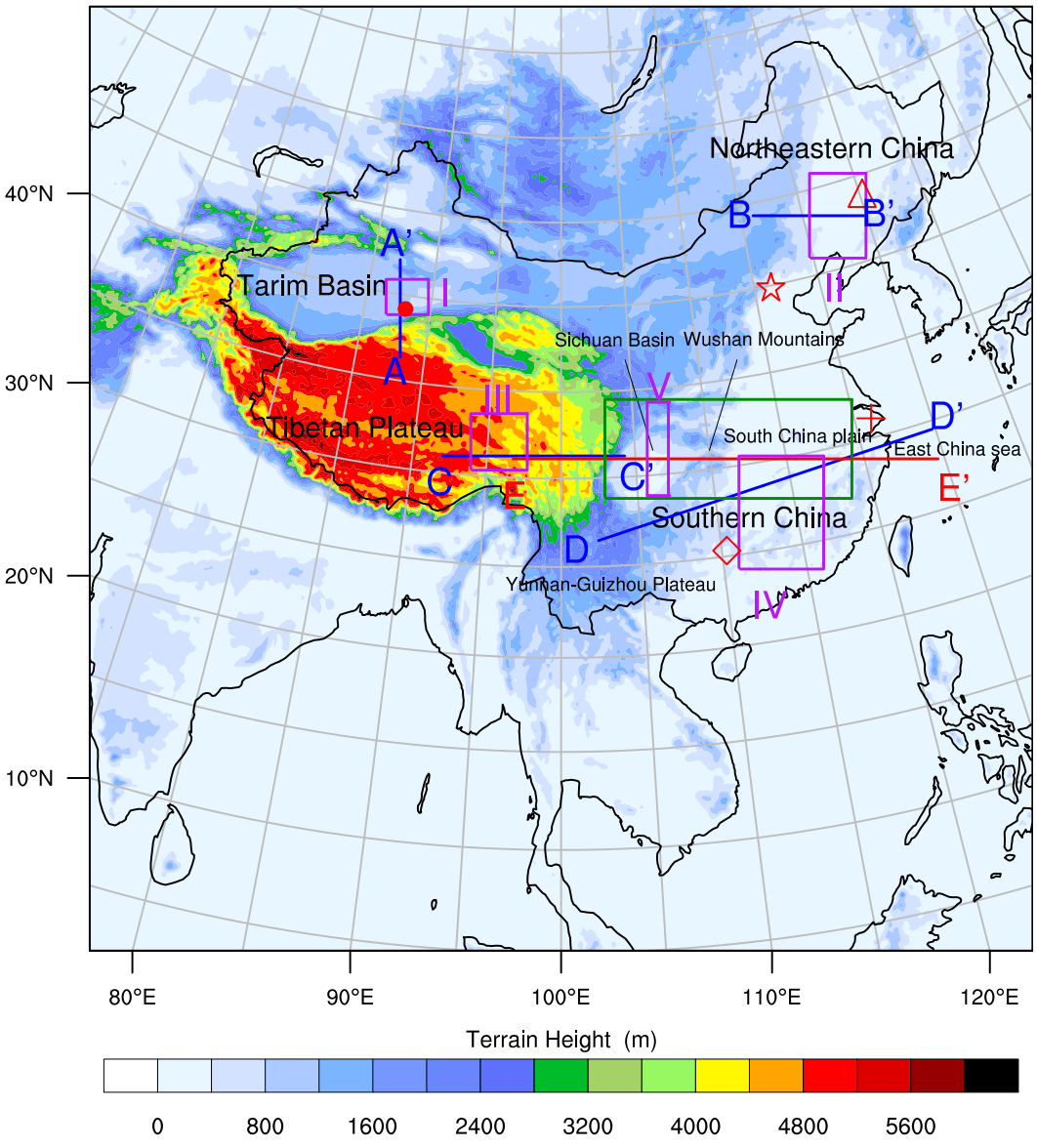

FIG. 1. The simulation domain with the model terrain height (shading, m), cross sections (blue lines), regional areas (purple and green boxes), and observation sites (red dot, Ruoqiang; red five-pointed star, Beijing; red cross, Qingpu; red triangle, Changchun; red diamond, Guilin).

day, the model is initialized at 0000 UTC for a 36-h simulation. Hourly model data for later periods of each simulation (23 or 25 h) are used as shown in Fig. 2. For the commencing time of daily outputs we chose to vary between 1200 and 0600 UTC with the corresponding end time as between 1100 and 0600 UTC. This method can smooth out the discontinuities for statistics between successive runs due to their different forecasting errors. The reinitialization by subdividing a long-term continuous integration into shorter ones is an effective method to alleviate the problem of systematic model error that may grow in a long-term integration (Lo et al. 2008), and the approach has been widely adopted (Žagar et al. 2006; Jiménez et al. 2010; Parish and Oolman 2010; Zhang et al. 2012). Figure 1 shows the simulation domain with model terrain; the model configurations are given in Table 1. Convective parameterization is applied in our 9-km resolution simulations because it is still needed for simulations at this gray-zone resolution (Yu and Lee 2010; Duda 2011).

To validate the model dataset, soundings from Beijing (June 2009), Ruoqiang (May–July 2006–11), Changchun (June and July 2010), and Guilin stations (June and July 2007–10)—indicated by the red five-pointed star, red dot,

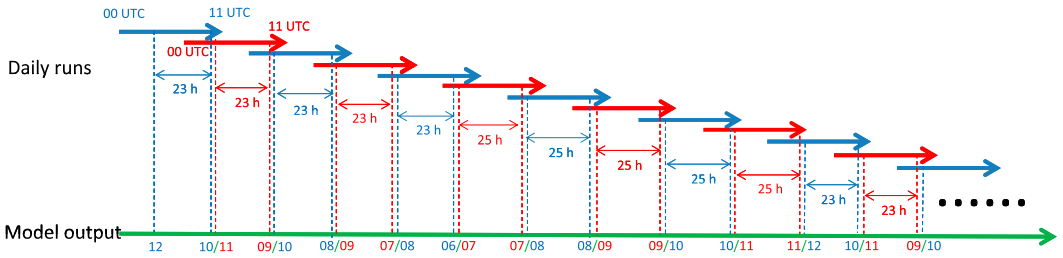

FIG. 2. The time flow diagram of daily simulations (blue and red arrows) and combination (a green arrow) of each daily model output for different period (blue and red dashed lines).

red triangle, and red diamond, respectively, in Fig. 1—and the wind profiler radar (WPR) observations with high vertical resolution at Qingpu (June and July 2010; indicated by a red cross in Fig. 1) are used.

b. *Criteria for identifying LLJs*

Previous statistical studies adopted various criteria for identifying LLJs (Bonner 1968; Chen and Yu 1988; Rife et al. 2010). However, recent studies, following the study by Bonner (1968), adopt criteria by defining threshold values for the maximum wind speed, height of maximum wind, and magnitude of required vertical shear above the jet (Mitchell et al. 1995; Whiteman et al. 1997; Chen et al. 2005; Pham et al. 2008; Du et al. 2012).

Over mainland China, most researchers have identified LLJs based on the maximum horizontal wind speed at the 925-, 850-, or 700-hPa levels without requiring a threshold value for the vertical shear of the horizontal winds, due to limitations of data resolution (e.g., Tao and Chen 1987). In this study, the high-resolution model data allow us to consider the vertical shear of horizontal wind for identifying the LLJs, including both BLJs and SLLJs. The following criteria are used: 1) the maximum wind speed is more than $10\,\mathrm{m\,s^{-1}}$ in the lowest 15 layers of the model (below 4 km) and 2) the wind speed must decrease by at least $3\,\mathrm{m\,s^{-1}}$ from the height of the wind maximum to the wind minimum above that. These criteria are similar to those adopted by Du et al. (2012), Pham et al. (2008), and Whiteman et al. (1997). The criterion requiring LLJs to have a significant vertical shear of horizontal wind ensures that these jets have jetlike profiles. To provide a larger LLJ sample to compile statistics, the criterion for maximum wind speed is relatively low. We define the height of the LLJs as the height of the horizontal wind speed maxima where the LLJs occur. The LLJ direction is defined as the wind direction at the height of the LLJ. In this study, we follow the approach of Du et al. (2012) and classify LLJs in China into BLJs (occurring below the 8th layer, approximately below the 1-km level) and SLLJs (occurring between the 8th and 15th layers, approximately between the 1-km and 4-km levels). It is possible for a BLJ and an SLLJ to occur at the same time with a double peak, although this does not occur very often (below 5%). When the double peak occurs, both peaks are counted.

In this paper, we also defined BLJ (SLLJ) events and BLJ (SLLJ) days over a certain region. A SLLJ (BLJ) event is defined as an hour with more than 25% grids in a certain region satisfying the SLLJ (BLJ) criteria. A BLJ (SLLJ) day is defined as a day that has more than six hours (not required to be consecutive) satisfying the BLJ (SLLJ) event criteria over a certain region.

c. *Momentum balance analysis*

In this paper, the momentum balance analysis is adopted to investigate the mechanism for the diurnal variations of LLJs. The horizontal momentum equation can be written as

$$\frac{\partial u}{\partial t} = \left(-u\frac{\partial u}{\partial x} - v\frac{\partial u}{\partial y}\right) - \frac{\partial \Phi}{\partial x} + fv + F_x, \tag{2.1}$$

$$\frac{\partial v}{\partial t} = \left(-u\frac{\partial v}{\partial x} - v\frac{\partial v}{\partial y}\right) - \frac{\partial \Phi}{\partial y} - fu + F_y, \tag{2.2}$$

or

$$\frac{\partial u}{\partial t} = \left(-u\frac{\partial u}{\partial x} - v\frac{\partial u}{\partial y}\right) + f(v - v_g) + F_x, \tag{2.3}$$

$$\frac{\partial v}{\partial t} = \left(-u\frac{\partial v}{\partial x} - v\frac{\partial v}{\partial y}\right) - f(u - u_g) + F_y. \tag{2.4}$$

Term I Term II Term III Term IV

TABLE 1. Configurations of the WRF Model used in this study.

Numerical and physical process	Schemes and model
Microphysics	WRF single-moment (WSM) 6-class graupel
Longwave radiation	Rapid Radiative Transfer Model (RRTM) scheme
Shortwave radiation	Dudhia scheme
Surface layer	Monin–Obukhov
Land surface	Unified Noah land surface model
Planetary boundary layer	Yonsei University (YSU)
Cumulus parameterization	Kain–Fritsch

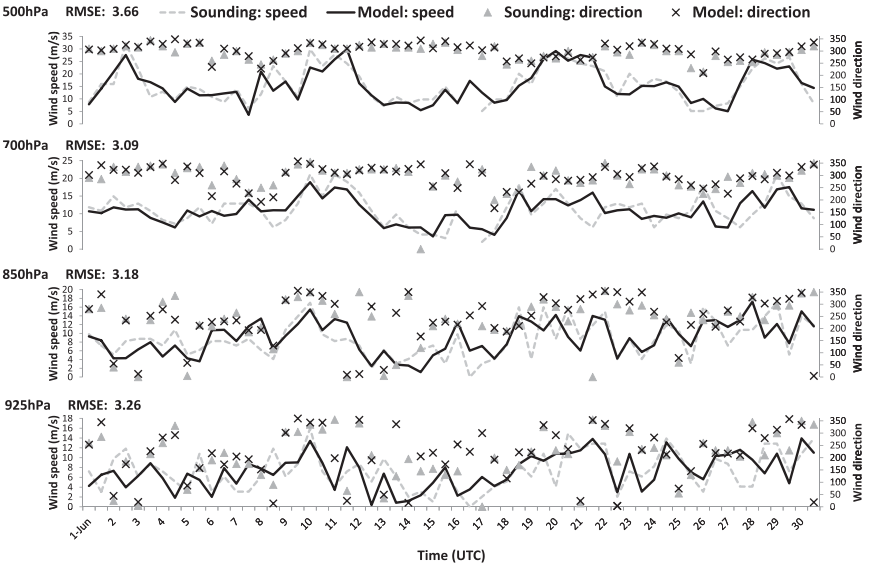

FIG. 3. Time series of wind speeds and directions at Beijing station (39.93°N, 116.28°E) at 925-, 850-, 700-, and 500-hPa levels for 0000 and 1200 UTC June 2009 from sounding observations (gray dashed lines; gray triangles) and model data (black solid lines; black crosses) with rms errors of the wind speeds.

Equations (2.3) and (2.4) state that the local acceleration of the u and v wind component (term I, tendency) equals the sum of horizontal advection in the x and y directions (term II), the Coriolis force acting on ageostrophic wind in the x and y directions (term III), and friction in the x and y directions (term IV, residual term). In the model, term IV is the residue from the equation. Term IV comprises friction, vertical advection, and uncertainties. The vertical advection is rather small and the frictional force is the dominant term in term IV. Because the directions of some LLJs are not in the x or y direction, it is desirable to transform horizontal momentum from (x, y) coordinates into right-hand coordinates (x', y'), with the y' axis pointing to the direction of LLJ (Zhang et al. 2003). Therefore,

$$v' = u\sin\varphi + v\cos\varphi, \tag{2.5}$$

where v' is the wind speed in the y' axis direction and φ is the angle between the y' axis and the y axis.

The momentum balance for the y' direction can be written by the following transformation equations:

$$\text{Term I} = \frac{\partial u}{\partial t}\sin\varphi + \frac{\partial v}{\partial t}\cos\varphi, \tag{2.6}$$

$$\text{Term II} = \left(-u\frac{\partial u}{\partial x} - v\frac{\partial u}{\partial y}\right)\sin\varphi + \left(-u\frac{\partial v}{\partial x} - v\frac{\partial v}{\partial y}\right)\cos\varphi, \tag{2.7}$$

$$\text{Term III} = f(v - v_g)\sin\varphi - f(u - u_g)\cos\varphi, \tag{2.8}$$

$$\text{Term IV} = F_x\sin\varphi + F_y\cos\varphi. \tag{2.9}$$

Based on inertial oscillation proposed by Blackadar (1957), strong vertical mixing in the boundary layer during the daytime results in ageostrophic winds and clockwise rotation of the ageostrophic winds attributed to the diurnal variation of LLJ. Therefore, if inertial oscillation is the main mechanism for the diurnal cycle of LLJ, term III should be a dominant term in the momentum balance and term IV also should contribute to the deceleration of the LLJ in the boundary layer during the daytime.

3. Evaluation of the model dataset

Before using the model dataset for diagnostic studies it is necessary to validate the model results with observations. First, we compared the WRF Model output of winds with that of sounding observed winds from the Beijing station (54511: 39.93°N, 116.28°E, denoted by a red star in Fig. 1) in June 2009. Figure 3 shows the time series of wind speeds and directions from the model simulations and soundings at 0000 and 1200 UTC at the 925-, 850-, 700-, and 500-hPa levels for June 2009. It is evident that the model dataset is in reasonably good agreement with observations. The rms error (RMSE) of

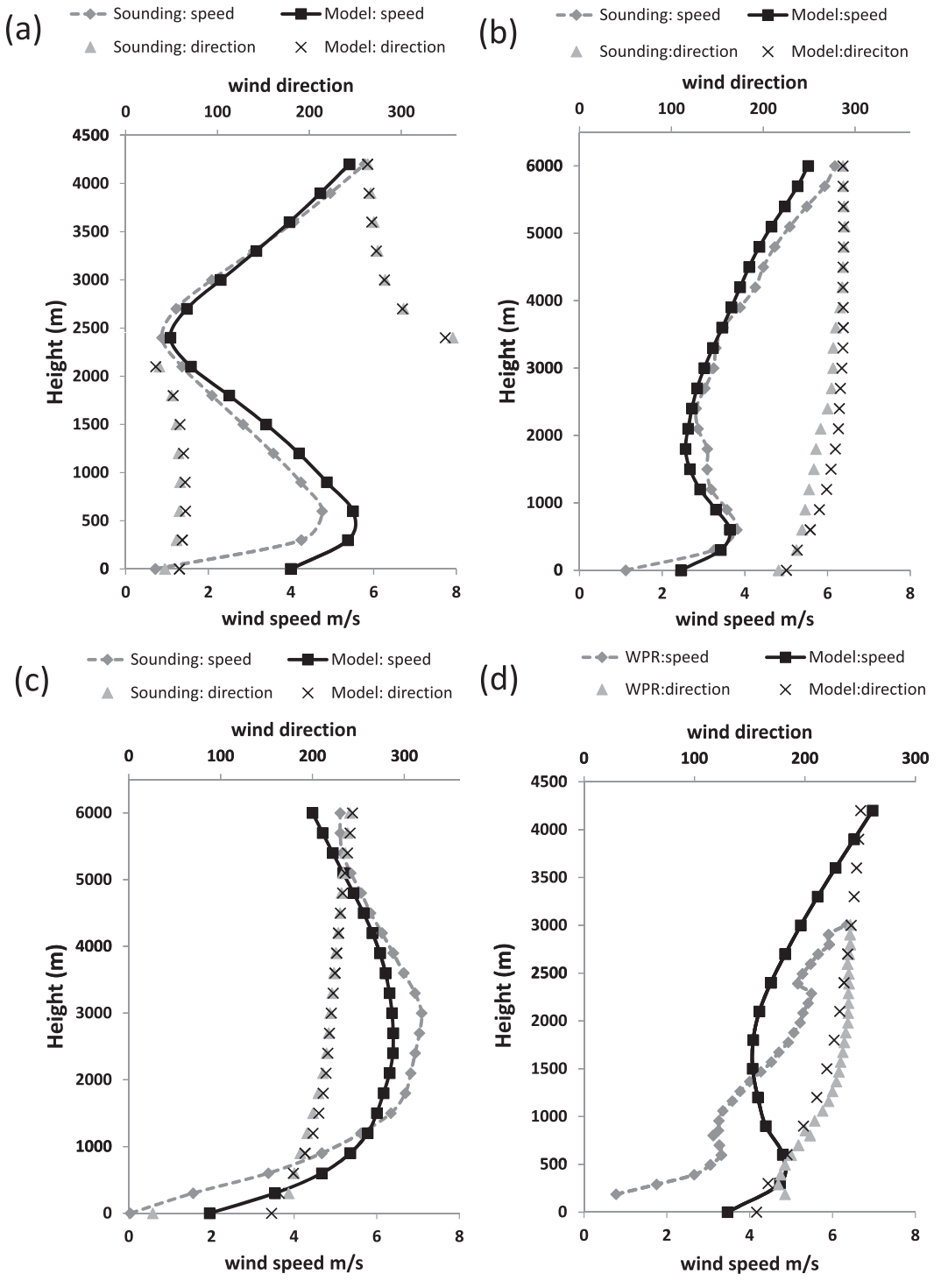

FIG. 4. Mean vertical wind speed ($m\,s^{-1}$) and direction (°) profiles from observations (gray dashed line for wind speed, gray triangle for wind direction) and the model data (black solid line for wind speed, black cross for wind direction) at (a) Ruoqiang (sounding, averaged May–July 2006–11), (b) Changchun (sounding, averaged June and July 2010), (c) Guilin (sounding, averaged June and July 2007–10) and (d) Qingpu (wind profiler radar, averaged June and July 2008–09) stations.

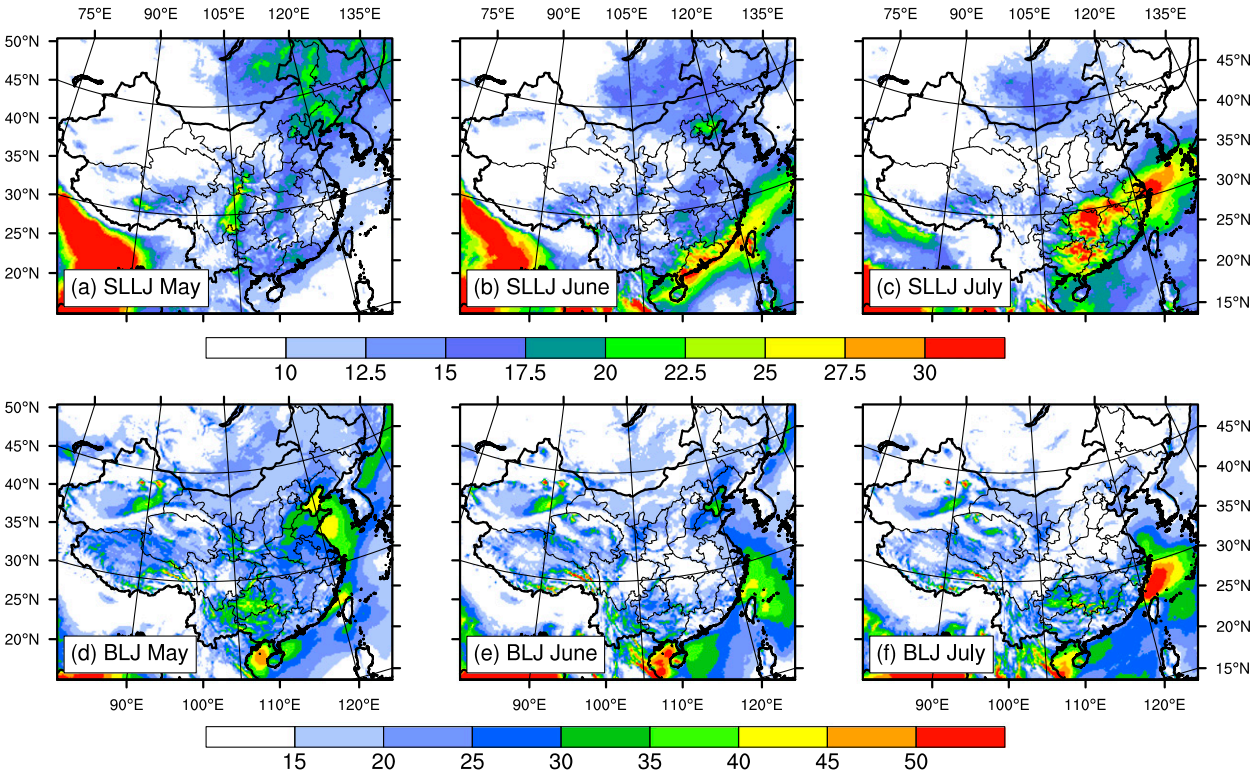

FIG. 5. Horizontal distributions of occurring frequencies (shading, %) of (top) SLLJs and (bottom) BLJs in China for (a),(d) May, (b),(e) June, and (c),(f) July averaged from 2006 to 2011.

wind speed is about 3–4 m s^{-1}. Because Rife et al. (2010) suggested that LLJs frequently occur at Tarim basin, we also compare the mean wind profiles from model output with high vertical resolution sounding observations (raw data) at Ruoqiang station (51777: 39.03°N, 88.16°E, denoted by a red dot in Fig. 1) in that region. The model output provides a good overall depiction of LLJs at Ruoqiang with the height of the jet core at the 600-m level above the ground, consistent with the observations (Fig. 4a). The model output tends to overestimate the low-level mean wind speed, especially for surface winds. We also evaluate model-simulated wind profiles (speed and direction) at Changchun (54161: 43.9°N, 125.22°E, denoted by a red triangle in Fig. 1), Guilin (57957: 25.32°N, 110.3°E, denoted by a red diamond in Fig. 1), and Qingpu (31.1°N, 121.1°E, denoted by a red cross in Fig. 1) with soundings or WPR observations (Figs. 4b–d). The different averaging period used for each station location is dictated by the available high vertical resolution measurements at each site. The model output at these three stations provides a good depiction of mean vertical wind profiles as well, except for the surface winds. The model appears to perform relatively poorly in simulated wind speed at Qingpu, partially because of possible speed bias at the site. Overall, the model simulation adequately replicates the time series of winds and also the mean vertical wind profiles at these sites.

4. Spatial distributions of low-level jets

a. Horizontal distributions of LLJ occurrences

Figure 5 shows the horizontal distributions of the occurrences of SLLJs and BLJs in China during May–July from the high temporal and spatial resolution model output. We found that the occurrences of LLJs are relatively frequent for southern China, Tarim basin, the Tibetan Plateau (TP), and northeastern China. The first three regions are consistent with studies by Rife et al. (2010), Liu et al. (2012), and Wang et al. (2013). The northeastern China region is a newly identified location and has not been previously studied.

There are some differences between the horizontal distributions of SLLJs and BLJs. SLLJs are frequent over southern China and northeastern China (Figs. 5a–c). Previous studies suggested that the increase in SLLJ occurrence during the mei-yu period is a notable feature

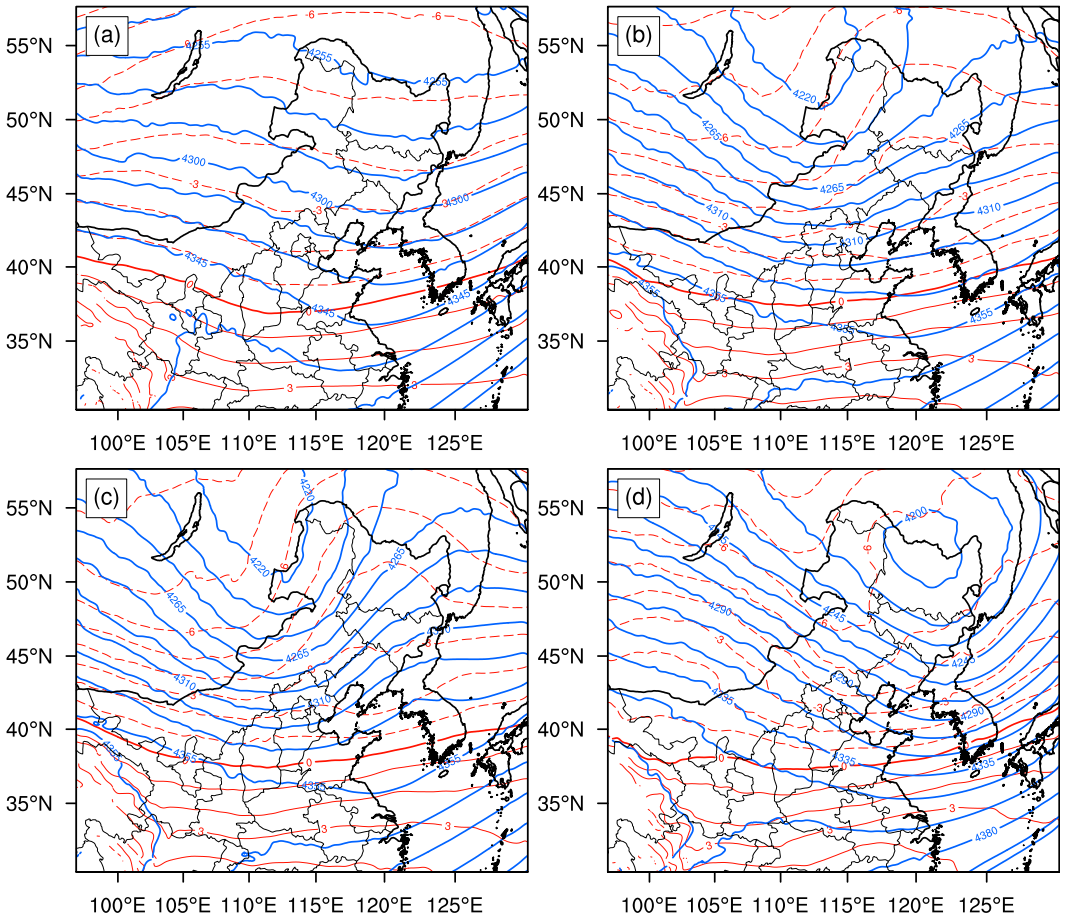

FIG. 6. The averaged 600-hPa geopotential height (blue solid line, gpm) and temperature (red dashed line, °C) for June 2006–11: (a) non-SLLJ event events, (b) SLLJ events, (c) southwesterly SLLJ events, and (d) northwesterly SLLJ events over northeastern China.

over southern China (Tao and Chen 1987; Du et al. 2012). We found that the maximum occurrence of SLLJs in southern China shifts northward from May to July due to the northward shift of the mei-yu front. The SLLJs over southern China during the mei-yu season are related to the mei-yu front. A SLLJ (BLJ) event over northeastern China is defined as more than 25% grids within the purple box II (Fig. 1), satisfying the SLLJs (BLJs) criteria based on hourly model data. The frequency of SLLJs events over northeastern China in June is 15.3%. In Figs. 6a and 6b, we compared the mean 600-hPa geopotential height and temperature for non-SLLJs events and those for the SLLJs events over northeastern China in June. We found that SLLJs over northeastern China are closely related to the low pressure systems or trough with a cold core. The northeast cold vortex (NECV), a closed cyclonic circulation with a cold core at the midlevel (35°–60°N, 115°–145°E), is a major high impact weather system in northeastern China that occurs mainly in May and June (Zhang et al. 2008; Zhang and Li 2009). SLLJs over northeastern China occur more frequently in May and June than July, which is in agreement with the seasonal variations of NECV occurrence (Figs. 5a–c). The SLLJs over northeastern China are associated with the NECV.

In China, the BLJs frequently occur in the coastal areas where a land–sea temperature gradient exists (coastal areas in southeastern China), adjacent to high terrain such as Tarim basin and the eastern Yunnan-Guizhou Plateau, and over the TP (Figs. 5d–f). Burk and Thompson (1996) suggested that the summertime northerly BLJs frequently found along the California coast are a result of baroclinity created by the juxtaposition of a heated continent and the cool marine layer. LLJs frequently occur adjacent to high terrain in different locations around the world, such as the Great Plains BLJs east of the Rocky Mountains (e.g., Bonner 1968) and South American BLJs on the eastern side of the Andes

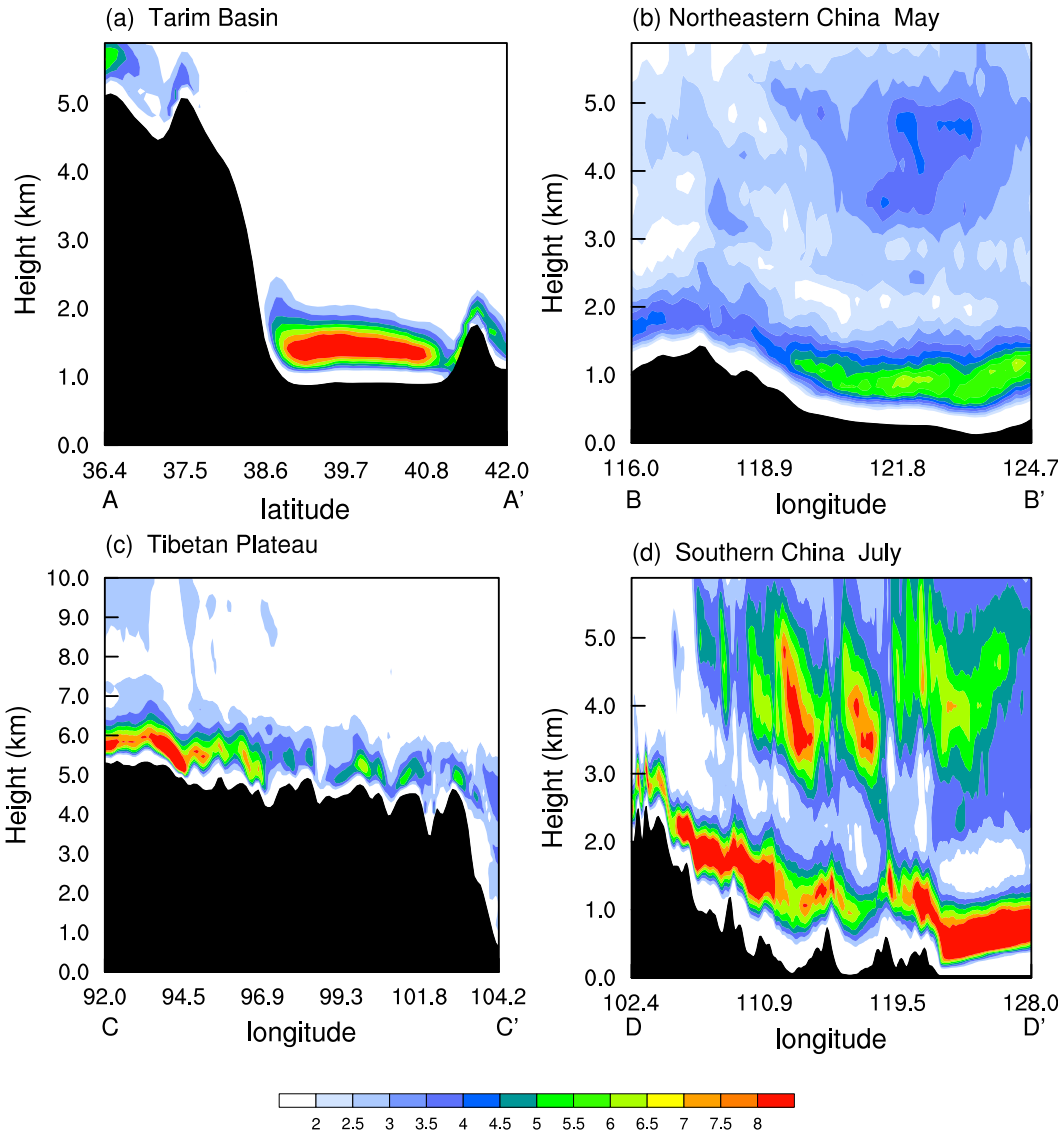

FIG. 7. Vertical cross sections of the frequencies of the LLJs (shading, %) for (a) the Tarim basin, (b) northeastern China in May, (c) the Tibetan Plateau, and (d) southern China in July along the blue lines (A–A′, B–B′, C–C′, and D–D′) in Fig. 1.

(Marengo et al. 2004). Rife et al. (2010) found that nocturnal LLJs (BLJs) frequently occur over the TP and Brazilian highlands. Furthermore, the BLJs are also often found over northeastern China in May and over southern China in July where SLLJs occur frequently (Figs. 5d,f).

b. *Vertical distribution of LLJ occurrences*

Figure 7 shows the vertical distribution of LLJ occurrences below the 6-km level above sea level along AA′, BB′, CC′, and DD′ over the Tarim basin, northeastern China, the TP, and southern China, respectively (denoted by blue lines in Fig. 1). The main reason why the frequencies are smaller in the cross-sectional plots (Fig. 7) than the plan-view plots (Fig. 5) is because the plan-view plots are a vertical integral of frequencies above each grid point. Only BLJs occur over the Tarim basin and TP with a maximum frequency below the 1-km level above the ground level (AGL) (Figs. 7a,c). The vertical cross section along CC′ through northeastern China for May and along BB′ through eastern Yunnan-Guizhou Plateau, southeast China, and the coastal region for July show that there are double peaks in the vertical distribution of LLJ occurrences (Figs. 7b,d). The first peak is located at 700–800 m AGL and the second peak at 3–4 km AGL. Du et al. (2012) showed that LLJs

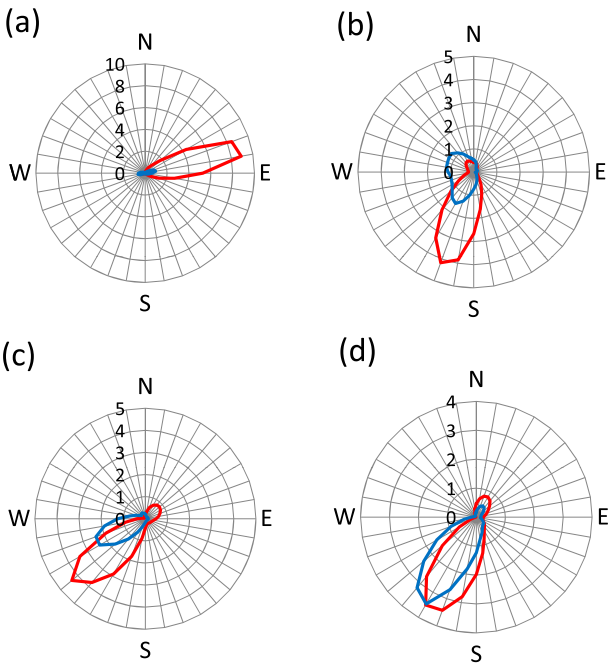

FIG. 8. Frequency distributions (%) of BLJ (red) and SLLJ (blue) directions averaged over four regions: (a) the Tarim basin (purple box I in Fig. 1), (b) northeastern China (purple box II in Fig. 1), (c) the Tibetan Plateau (purple box III in Fig. 1), and (d) southern China (purple box IV in Fig. 1).

in Shanghai occur frequently at both 500–800-m and 2100–2200-m levels. The model output captures the double-peak structure in agreement with observations in Shanghai. The first peak could be related to the frequent occurrences of BLJs over regions where the terrain height gradient (e.g., eastern Yunnan-Guizhou Plateau or northeastern China) or land–sea temperature gradient (e.g., coastal region of southeastern China) exists. The altitude of the second peak from model data is higher than that from wind profiler radar observations, probably because the vertical range of wind profiler radar data is limited to 3 km AGL. The second peak over northeastern China can be attributed to the frequent occurrence of SLLJs attributed to the NECV whereas the second peak over southern China may be due to the mei-yu front. BLJs also occur frequently with large horizontal pressure gradients in the lower level (Du et al. 2012) so that BLJs in southern China increase from May to July when the mei-yu front shifts to southern China.

c. *Frequency distributions of LLJ direction*

BLJs over the Tarim basin are mainly easterlies (Fig. 8a), whereas BLJs over the TP have mostly westerly and southwesterly winds (Fig. 8c). Both BLJs and SLLJs over southern China are southwesterlies (Fig. 8d). BLJs over northeastern China are southwesterlies whereas SLLJs over northeastern China have either northwesterly or southwesterly winds (Fig. 8b) due to the eastward movement of the NECV (Figs. 6c,d). A schematic diagram summarizing the LLJ locations, heights, directions, and their relationship with the mei-yu front or NECV is given in Fig. 9.

5. Diurnal variations of low-level jets in China

Mean time–height cross sections of LLJs occurrences over the Tarim basin, TP, northeastern China, and southern China (four purple boxes in Fig. 1) are shown in Fig. 10. BLJs exhibit pronounced diurnal variations with a nocturnal/early morning maximum in all four regions. SLLJs in southern China show diurnal variations with a maximum at noon, whereas SLLJs over northeastern China have little diurnal variation. The reasons for the diurnal variations of BLJ and SLLJ occurrences will be discussed in sections 5a and 5b.

a. *Diurnal variations of BLJ occurrences*

Most of the BLJs in the Tarim basin are easterlies (Fig. 8a) and the peak in BLJ occurrence is close to the 850-hPa level (Fig. 7a, about 600 m AGL). The diurnal variations of the mean 850-hPa u component and the geostrophic wind component for the x direction (U and U_g) averaged over the Tarim basin area (denoted by purple box I in Fig. 1) for the 2006–11 early summer are shown in Fig. 11a. It is found that the u component has a (negative) minimum at 0100 LST, which coincides with the nocturnal maximum in BLJ occurrence. The geostrophic wind component, U_g, exhibits little diurnal variation. Therefore, the variations are mainly attributed to the diurnal variations of ageostrophic winds. Southerly ageostrophic wind in the afternoon is a result of strong vertical mixing (friction) in the boundary layer (Figs. 11b and 12). The ageostrophic wind veers to easterly at night (0000–0300 LST) (Fig. 11b) resulting in a diurnal minimum of U. Such clockwise rotation of ageostrophic winds (Fig. 11b) suggests that the inertial oscillation mechanism described by Blackadar (1957) is responsible for the nocturnal BLJ maximum over the Tarim basin.

The momentum balance for the x direction [Eq. (2.3)] at the 850-hPa level is analyzed to investigate the mechanism for the diurnal variations of BLJs over Tarim basin. Figure 12 shows the diurnal variations of the four terms in Eq. (2.3). Diurnal variations of horizontal advection (term II) are relatively small compared to the other terms. During daytime, the friction term (residual term) is mainly responsible for the speed reduction in U, perhaps due to vertical momentum mixing in the planetary boundary layer. At night and in the early morning,

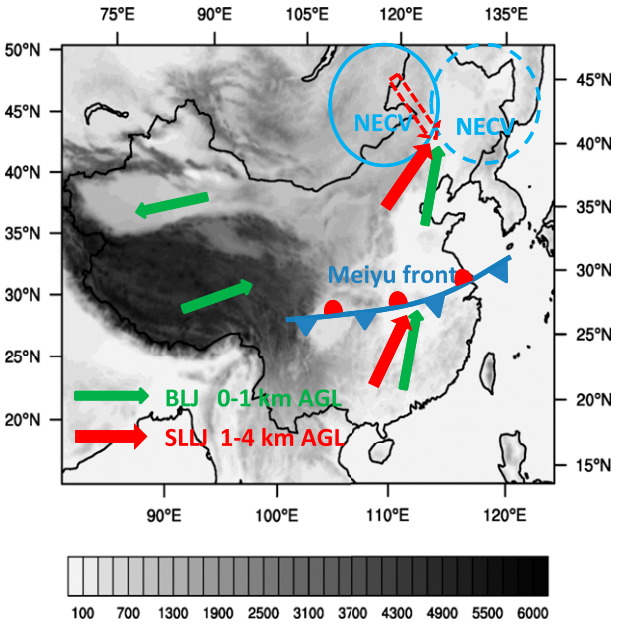

FIG. 9. A schematic diagram showing the locations, heights, and directions of BLJs (green arrows) and SLLJs (red arrows) along with the locations of the Mei-yu front and NECV during the early summer.

the Coriolis force acting on the ageostrophic wind in the x direction (term III) mainly accounts for the acceleration of the u component. Thus, the inertial oscillation (Coriolis force acting on ageostrophic wind) during nighttime, proposed by Blackadar (1957), and vertical mixing in the boundary layer (friction) during daytime can account for the diurnal variation of BLJs in the Tarim basin. The diurnal variations of BLJs over the TP are also analyzed, and the results are similar to that of the Tarim basin (not shown).

We next explore the diurnal variations of BLJs over northeastern China and southern China where both BLJs and SLLJs exist and BLJs might be affected by the NECV or mei-yu front. Because wind directions at low levels over northeastern China vary considerably due to variations in synoptic weather patterns, the diurnal variations of mean wind at the 900-hPa level for BLJ days over northeastern China and the associated momentum balance are investigated first. A BLJ day over northeastern China is defined as a day that has more than six hours satisfying the BLJ event criteria over northeastern China (purple box II in Fig. 1). Because BLJs over northeastern China are mostly southwesterly (210°) (Fig. 8b), the coordinate transformation ($\varphi = \pi/6$) is done as described in section 2c. The wind speed for the y' axis direction (v') equals $u\sin(\pi/6) + v\cos(\pi/6)$. As shown in Fig. 13a, the diurnal peak of v' (2300 LST) is nearly consistent with the diurnal peak of BLJ occurrence (0000 LST) over northeastern China. The geostrophic wind exhibits little diurnal variation. Figure 13b shows the diurnal variations of the four terms with coordinate (x', y') transformations [Eqs. (2.6)– (2.9)] for BLJ days over northeastern China. Generally, the Coriolis force acting on the ageostrophic wind (term III) and friction (term IV, residual term) mainly account for the diurnal variations of v'. Term III plays a role in accelerating v' during the entire day, whereas term IV mainly decelerates v' in the daytime. The diurnal variations of BLJs over southern China (box IV in Fig. 1) are analyzed in the same way ($\varphi = \pi/9$). We found that terms III and IV are also important terms in the momentum equation (Fig. 14). Overall, the diurnal variations of BLJs over the four regions are all mainly caused by inertial oscillation at nighttime and vertical mixing in the boundary layer during the daytime.

b. *Diurnal variations of SLLJ occurrences*

SLLJs are associated with synoptic- and subsynoptic-scale weather systems, such as the NECV or mei-yu front (Tao and Chen 1987; Chen et al. 1994; Zhang and Li 2009; Du et al. 2012). The diurnal variations of SLLJs over northeastern China are small (Fig. 10b)—consistent with the small diurnal variations of the corresponding NECV. However, SLLJs over southern China show notable diurnal variations (Fig. 10d) and will be examined in this section.

Previous studies suggested that the increase in SLLJ occurrence is a notable feature during the mei-yu period and that the SLLJs are closely related to the development of the mesoscale convective systems (MCSs) embedded along mei-yu fronts and warm season precipitation (Matsumoto et al. 1971; Akiyama 1973; Tao and Chen 1987; Chen and Yu 1988; Du et al. 2012). The diurnal variation of warm season precipitation east of the eastern TP has been studied extensively (e.g., Xu and Zipser 2011; Bao et al. 2011). The local peak phase of diurnal precipitation begins in the mid to late afternoon on the eastern edge of the TP, which subsequently propagates eastward at an average speed of 13 m s^{-1} (Bao et al. 2011). Diurnal variations of SLLJs may be related to the diurnal variations of corresponding synoptic- and subsynoptic-scale weather systems, which have not been well documented in previous studies. Sun and Zhang (2012) suggested that the LLJ to the south of mei-yu front is much stronger during nighttime when precipitation is more intense and convective activity along the mei-yu front is more active than during daytime. Because precipitation has varying maximum diurnal peaks at different locations over southern China, a question arises: what do the diurnal variations of the SLLJs look like?

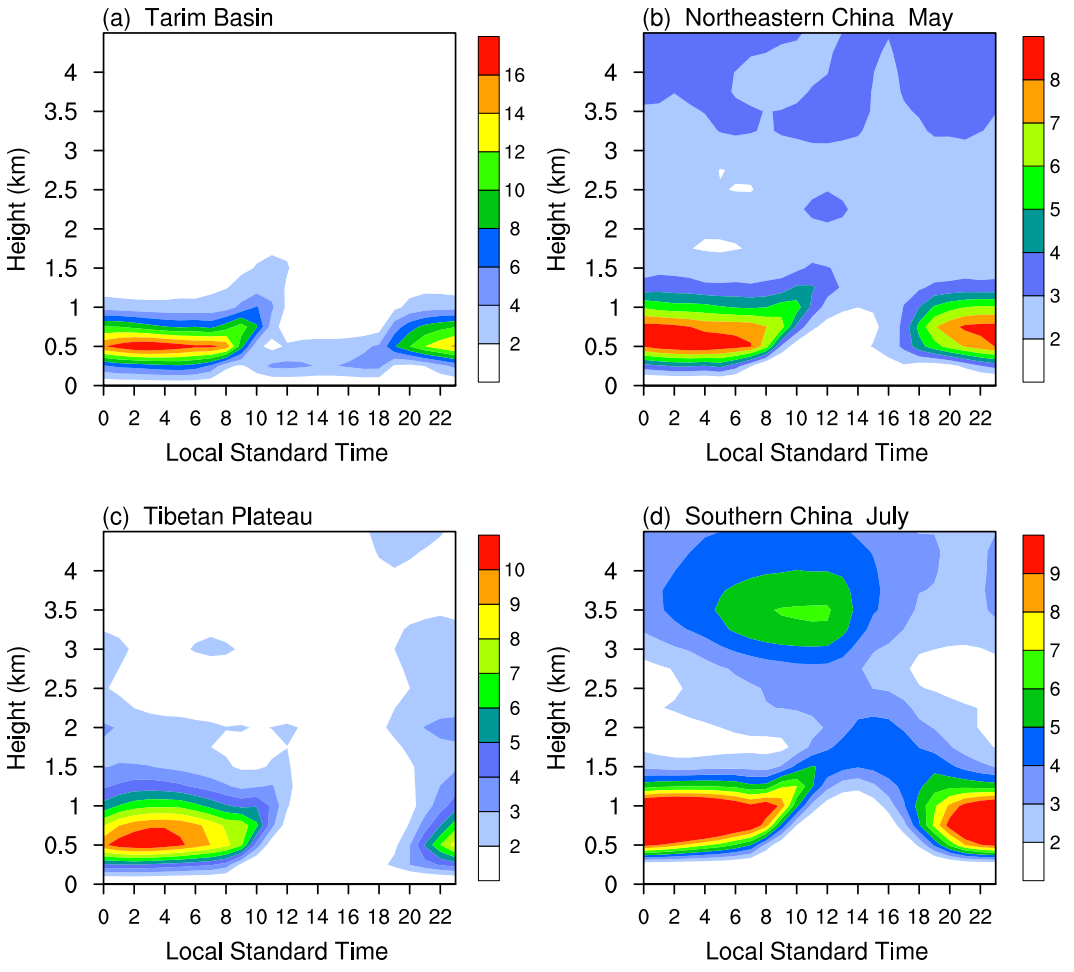

FIG. 10. Mean time–height plots of LLJ occurrences in four regions: (a) Tarim basin, (b) northeastern China, (c) the Tibetan Plateau, and (d) southern China, denoted by purple boxes in Fig. 1.

First, we examine whether our model simulation replicates the eastward propagation of local diurnal peak phase of precipitation as observed. Following He and Zhang (2010) and Bao et al. (2011), normalized hourly precipitation deviations are estimated as the mean precipitation rate at this hour minus the mean precipitation rate throughout the day, normalized by the standard deviation of hourly precipitation at each point. Figures 15a–c show longitude (x direction)–time Hovmöller diagrams of the normalized hourly precipitation deviation averaged from south to north over the green box in Fig. 1 for May, June, and July, respectively. The results of our model simulations are in agreement with the previous observational studies that the local diurnal peak phase of precipitation propagates eastward east of the TP (Wang et al. 2004; Bao et al. 2011; Xu and Zipser 2011). As shown in Fig. 15a, the diurnal variation peak begins to migrate eastward over the eastern edge of the TP (near 103°E) around 1200–1500 UTC (1900–2200 LST) and arrives at the Sichuan basin (SB, shown in Fig. 1) (near 106°E) around 1800–2100 UTC (0100–0400 LST). The diurnal precipitation peak continues to move eastward to the Wushan Mountains (WM, shown in Fig. 1) (112°E). Another eastward propagation starts east of the WM around 1500–1800 UTC (2300–0200 LT) and reaches 116°N around 0900 UTC (1700 LST). Another coexisting diurnal varying precipitation peak dominates over the South China Plain (SCP) during 0600–0900 UTC (1400–1700 LST). Therefore, two diurnal modes exist for the precipitation of southern China, the propagation mode and stationary mode, and have seasonal variations (Figs. 15a–c). The diurnal peak propagates farther eastward in May (to 112°E and emigrates to 116°E, Fig. 15a) and June (to 109°E, Fig. 15b) than in July (to 105°E, Fig. 15c), in agreement with Bao et al. (2011) and Xu and Zipser (2011). Hence, the eastward propagation of local diurnal peak phase of precipitation east of the TP and stationary diurnal phase over the SCP are reproduced in our model.

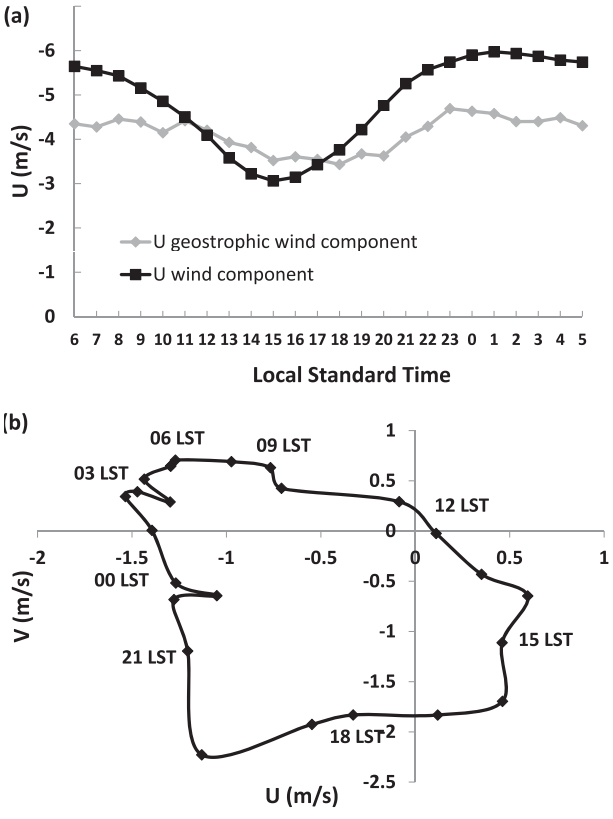

FIG. 11. (a) Diurnal variations of mean 850-hPa u component (U) and the geostrophic wind component for the x direction (U_g) averaged over the Tarim basin area. (b) Clockwise rotation of mean 850-hPa ageostrophic wind averaged over the Tarim basin area (purple box I in Fig. 1).

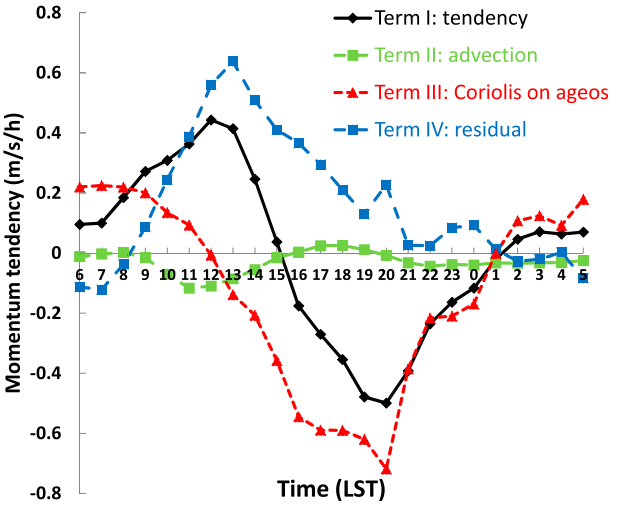

FIG. 12. Diurnal variations of individual terms in horizontal momentum equation at the 850-hPa level averaged over the Tarim basin area (purple box I in Fig. 1).

We would like to explore whether the diurnal variations of LLJs (including BLJs and SLLJs) are related to that of precipitation. The normalized hourly SLLJ (BLJ) occurrence deviations are defined as the mean occurrence frequency of SLLJs (BLJs) at this hour minus the mean occurrence frequency of SLLJs (BLJs) throughout the day, normalized by the standard deviation of hourly occurrence frequency of SLLJs (BLJs) at each point. Longitude (x direction)–time Hovmöller diagrams of hourly SLLJ occurrence deviation (Figs. 15d–f) and BLJ occurrence deviation (Figs. 15g–i) are plotted. In this region (the green box in Fig. 1), BLJs have a nocturnal occurrence maximum at nighttime or in the early morning (around 0200 LST) without any propagation. For the diurnal variations of SLLJs, there are two modes, the propagation mode and stationary mode. For the propagation mode, which is similar to precipitation, the diurnal peak of SLLJs propagates eastward and coincides with the diurnal peak of precipitation east of the TP. The propagation also covers a longer distance in May (to 112°E, Fig. 15d) and June (to 109°E, Fig. 15e) than in July (to 105°E, Fig. 15f), consistent with the seasonal change in the eastward propagation of precipitation except the remigration east of the WM in May is not as clear as that of precipitation. For the stationary mode that becomes the dominant mode after monsoon onset over SCP in mid-June, the diurnal peak of SLLJ occurs at noon (0400 UTC, 1200 LST) and precedes the peak of precipitation by a few hours.

Next, we would like to discuss the mechanisms for the propagation and stationary modes for the diurnal variations of precipitation and SLLJs. In May, before the monsoon onset, large-scale land–ocean thermal contrast is limited to low levels close to the land surface east of and above the TP with a prevailing westerly zonal wind in upper levels (Fig. 16a). After the onset of the summer monsoon in July, in addition to land–ocean contrast in low levels east of the TP, the atmosphere above the TP and SCP is characterized by rising motion and warmer temperature than over the ocean at the same level (Fig. 16b). The westerly zonal wind in the upper levels in July diminishes (Figs. 16a,b). Furthermore, the perturbation upward vertical motions in upper levels over SCP in the afternoon hours are more significant as the season progresses (Figs. 16c,d).

At low levels, we found three diurnally driven mountain–plain solenoidal circulation cells induced by differential heating: between the TP and the SB, between the WM and the SCP, and between the SCP and the East China Sea (ECS), for both May and July. At 0600 UTC, the perturbation upward (downward) vertical motions occur over the TP (SB), WM (east of WM), and SCP (ECS) (Figs. 16c,d) and vice versa for the 2100 UTC (Figs. 16e,f) owing to the diurnally driven thermal contrast due to the presence of the mountainous terrains.

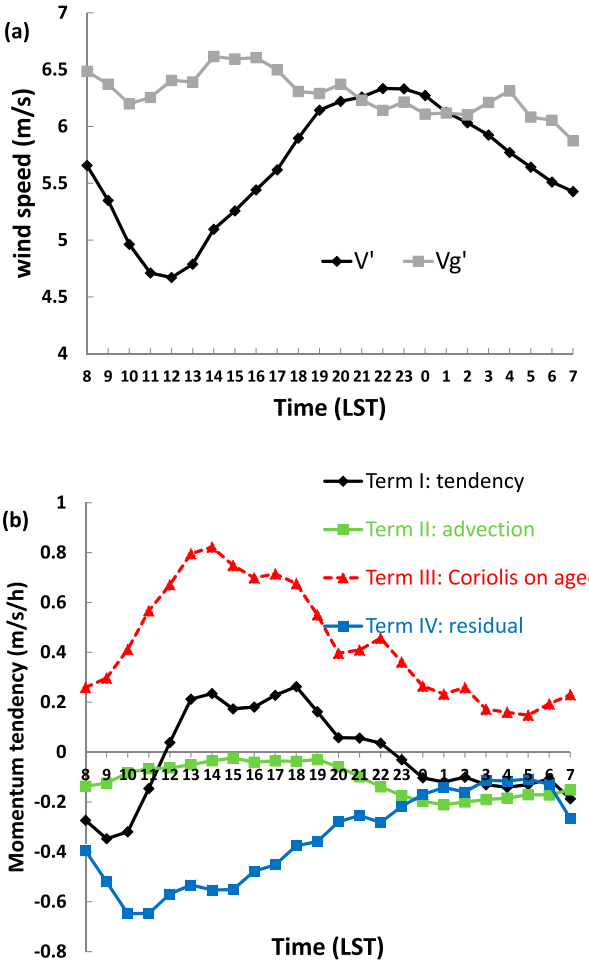

FIG. 13. Diurnal variations of (a) the mean wind component and geostrophic wind component for the y' direction for the BLJ days and (b) individual terms after coordinate transformation ($\varphi = \pi/6$) in the horizontal momentum equation at the 900-hPa level averaged over the purple box II in Fig. 1.

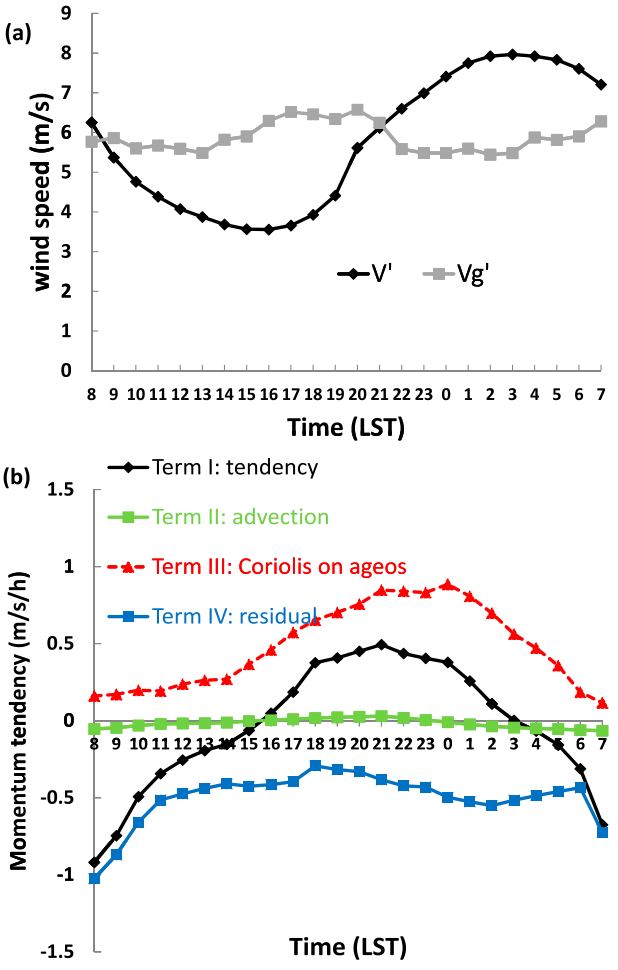

FIG. 14. Diurnal variations of (a) mean wind component and geostrophic wind component for the y' direction for the BLJ days and (b) individual terms after coordinate transformation ($\varphi = \pi/9$) in the horizontal momentum equation at the 925-hPa level averaged over the purple box IV in Fig. 1.

Figure 17 shows longitude (x direction)–time Hovmöller diagrams of vertical motion at the 450- and 800-hPa levels in May, June, and July. Similar to precipitation and SLLJs, vertical motions at the 450-hPa level also present both propagation and stationary modes and seasonal variations. The vertical motions at the 800-hPa level are diurnally driven, associated with local terrain (the TP, SB, WM, and the SCP), without significant seasonal variations.

In May, before the monsoon onset, the upward vertical motions above the TP and the WM develop in the afternoon (around 0600 UTC) (Fig. 16c). The upward motion aloft (Fig. 17a) and precipitation (Figs. 15a) propagate to the east of SB and SCP in the early morning due to the existence of an upper-level westerly zonal wind (Fig. 16a). Therefore, the two corresponding propagation modes of vertical motions at the 450-hPa level in May (Fig. 17a) (and precipitation) are initiated by the mountain–plain solenoidal circulations in low levels with strong zonal westerly wind aloft. At low levels (e.g., 800-hPa level), the diurnal variations of vertical motions are associated with the solenoidal circulations with the upward (downward) branches on the highland–plateau slopes and downward (upward) branches over the low basins or plains in the afternoon (early morning) (Figs. 16c,e and 17d).

In July, after monsoon onset, propagation of vertical motion in upper levels and precipitation become less significant (Fig. 17c). In contrast, with warming over SCP, the stationary mode of vertical motions over SCP with an afternoon (0600–0900 UTC) maximum is dominant (Figs. 16d, 17c), consistent with diurnal variation of precipitation at this time (Fig. 15c). The stationary mode of vertical motions in upper levels (Fig. 17c) is associated with large-scale differential heating between

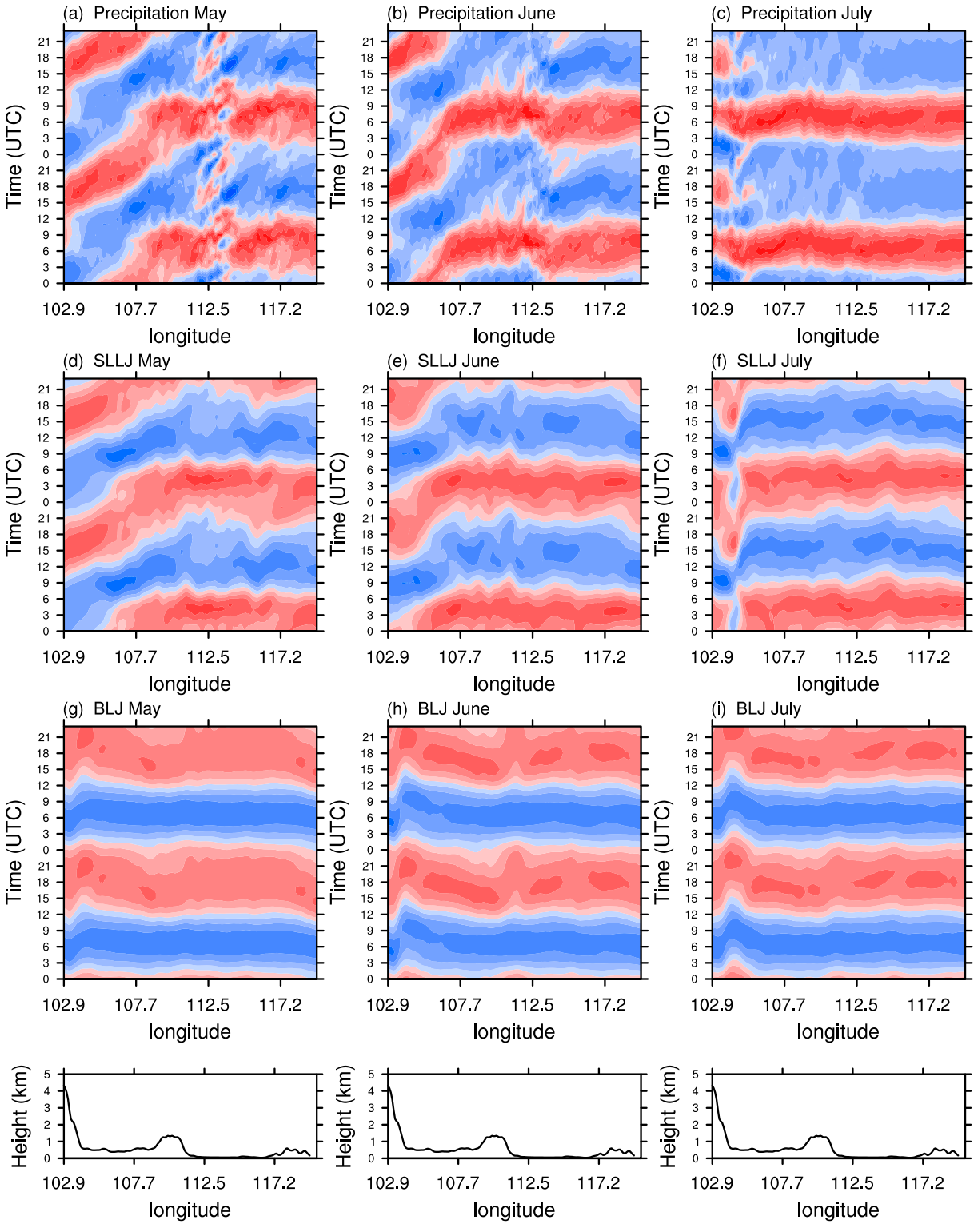

FIG. 15. Longitude (x direction)–time Hovmöller diagrams of the (a)–(c) normalized hourly precipitation deviations, (d)–(f) SLLJ deviations, and (g)–(i) BLJ deviations averaged from south to north over the green box in Fig. 1 in (left) May, (middle) June, and (right) July. The bottom panels show the average elevation along the east–west section.

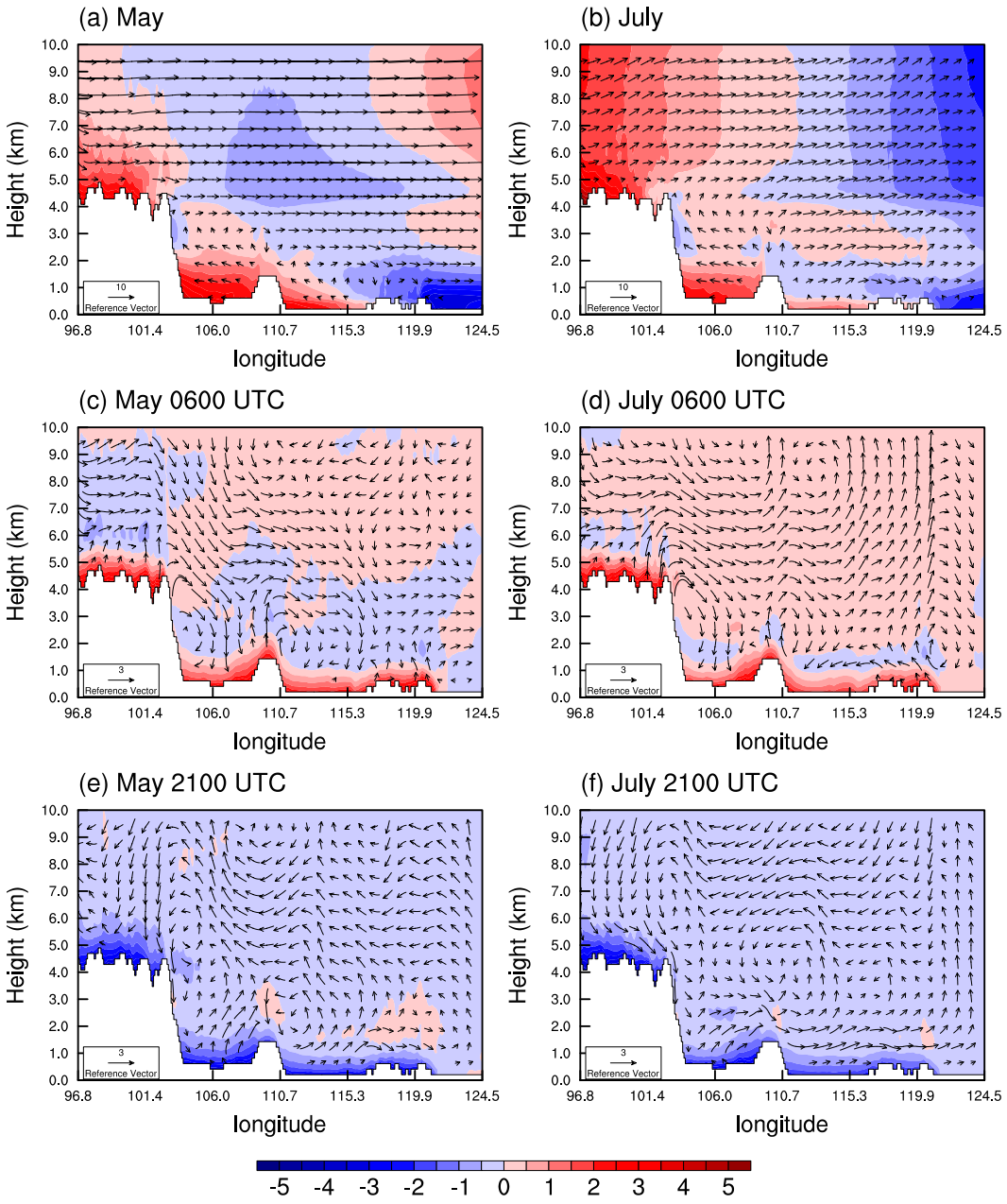

FIG. 16. Vertical cross sections of potential temperature zonal anomaly (shading, K) and vertical circulation vectors (zonal wind and 100 × vertical velocity, reference vector: m s^{-1}) along the red line E–E′ in Fig. 1 for (a) May and (b) July. Vertical cross sections of perturbation potential temperature (shading, K) and perturbation vertical circulation vectors (perturbation zonal wind and 100 × perturbation vertical velocity, reference vector: m s^{-1}) for May and July at (c),(d) 0600 and (e),(f) 2100 UTC. Note that the zonal anomaly potential temperature is defined by the deviation of potential temperature at each level from the zonal mean potential temperature for the cross section. The perturbation vertical circulation vectors (potential temperature) at 0600 and 2100 UTC are defined by the deviation of the 0600 and 2100 UTC vertical circulation vectors (potential temperature) from the daily mean vertical circulation vectors (potential temperature).

the TP/China Plain and the ocean (Fig. 16b) and becomes the dominant mode after the onset of the monsoon.

For the propagation mode east of the TP, the diurnal variations of SLLJs are closely related to those of precipitation due to the close relationship of SLLJs, synoptic or subsynoptic (MCS) systems, and precipitation. The development of SLLJs is closely linked to deepening of the mei-yu frontal cyclone to the east of

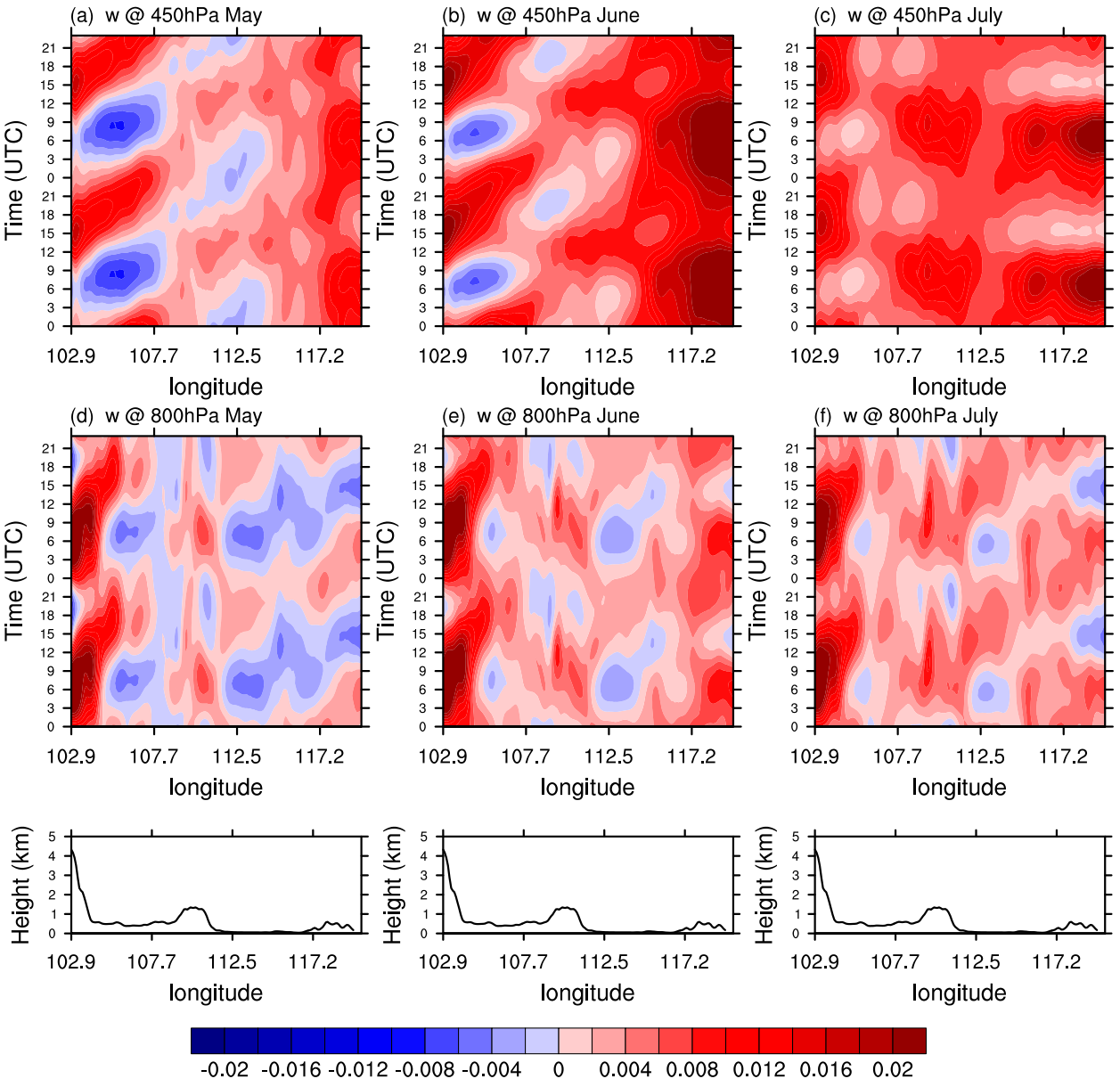

FIG. 17. Longitude (x direction)–time Hovmöller diagrams of vertical motion at the (a)–(c) 450-hPa and (d)–(f) 800-hPa levels averaged from south to north over the green box in Fig. 1 in (left) May, (middle) June, and (right) July. The bottom panels show the average elevation along the west–east section.

the TP in the presence of convective feedback (Chen 1982; Chen et al. 1994, 1997). The increasing pressure gradient force produced by the deepening of the mei-yu frontal cyclone can enhance SLLJs on the southeastern side of the cyclone (Chen et al. 1994; Chen and Chen 1995; Kato 1998; Davidson et al. 1998; Zhang et al. 2003).

The momentum balance of horizontal winds at the 600-hPa level over box V in May is analyzed after coordinate transformation ($\varphi = \pi/4$) (Fig. 18a). We found that the advection term (term II) is the dominant term for the diurnal variation of SLLJs over SB, consistent with the eastward propagation of SLLJ diurnal peak.

For the stationary mode over SCP, the diurnal peak of SLLJs (1100–1400 LST) leads that of precipitation (1400–1700 LST) by a few hours. Figures 19a–h shows perturbation wind fields and potential temperature at the 600-hPa level every 3 h during the diurnal cycle in July. The perturbation wind fields (potential temperature) every 3 h are defined by the deviation of the wind fields (potential temperature) at each time from the daily mean wind fields (potential temperature). The

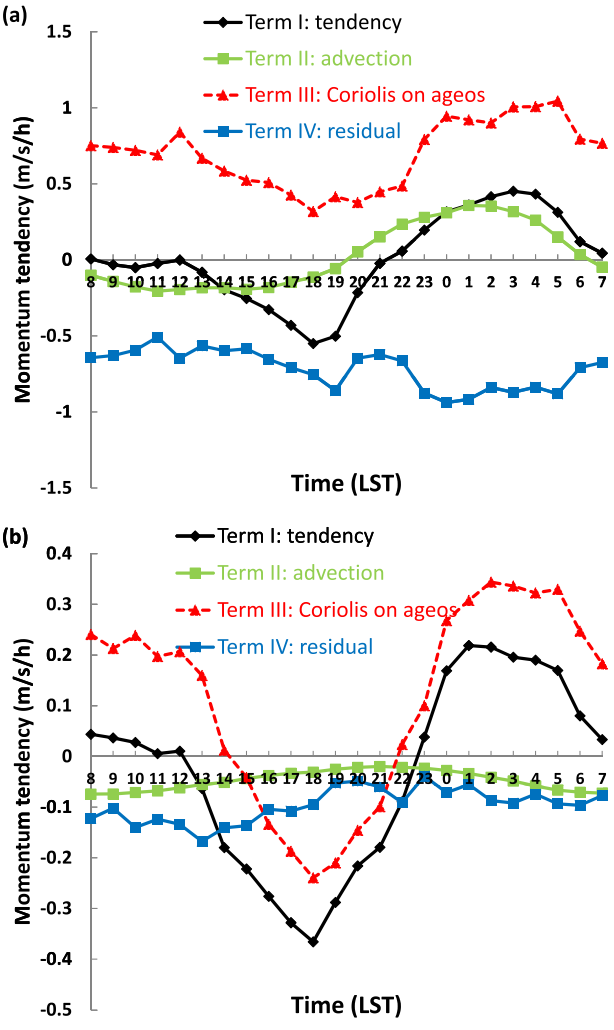

FIG. 18. Diurnal variations of individual terms after coordinate transformation ($\varphi = \pi/4$) in the horizontal momentum equation at the 600-hPa level averaged over the purple boxes (a) V and (b) IV in Fig. 1.

large-scale thermal difference between land and ocean in the afternoon (0600 UTC) leads to westerly perturbation winds at the 600-hPa level (Fig. 19d). The perturbation winds demonstrate veering during entire day (Fig. 19i) and veer to the southeast around 0300 UTC (1100 LST, Fig. 19f). This results in maximum wind at the 600-hPa level over the SCP, which contributes to the diurnal variation of SLLJs.

From the momentum balance analysis ($\varphi = \pi/4$) after the monsoon onset, the advection term (term II) and friction term (term IV, residual term) are not important, but Coriolis force acting on the ageostrophic wind (term III) is the dominant term for the diurnal variation of SLLJs over the SCP (Fig. 18b), which further suggests that the inertial oscillation mechanism in the presence of land–sea thermal contrast without friction is responsible for diurnal variation of SLLJs over the SCP (stationary mode).

6. Summary

Low-level jets (LLJs) have been studied extensively over many different parts of the world because of their close relationship with precipitation. However, given the limitations of observational data, detailed spatial distributions of LLJs in China are not well documented. In this study, long-term simulations over China using a high-resolution nonhydrostatic mesoscale model (WRF-ARW) with reinitialization by subdividing a long-term continuous integration into shorter ones (36 h) are used to produce a 6-yr dataset during the early summer (May–July from 2006 to 2011) with a grid spacing of 9 km and 40 vertical levels. After being evaluated, the model data are used to study the spatial distribution of LLJs in China and their diurnal variations.

The low-level jets can be classified into two types: 1) boundary layer jets (BLJs), which occur in the planetary boundary layer with significant vertical shear of horizontal winds and diurnal variations, and 2) synoptic-system-related low-level jet (SLLJs), which occur in the 600- to 900-hPa layer and are usually related to synoptic weather systems. These two types of LLJs have different characteristics and formation mechanisms (Du et al. 2012; Chen et al. 1994).

Over China, LLJs frequently occur in the following regions: the Tarim basin, southern China, northeastern China, and the Tibetan Plateau (TP). The SLLJs mainly occur over northeastern China and southern China and are associated with the Mei-yu front and northeast cold vortex (NECV), respectively. Over southern China, the maximum axis of SLLJ occurrences shifts northward from May to July, consistent with the seasonal migration of the mei-yu front. Over northeastern China, SLLJs occur more frequently in May and June than in July—consistent with the seasonal variations of NECVs. In addition, BLJs frequently occur over or next to high terrain, coastal areas, and in regions where SLLJs frequently occur. These areas include the Tarim basin, the TP, coastal areas of southeastern China, and the eastern Yunnan-Guizhou Plateau. The vertical structures of LLJ occurrences in northeastern China in May and southern China in July exhibit double peaks corresponding to the two types of LLJs (BLJs and SLLJs).

The BLJs in China all show notable diurnal variations with maximum occurrences at nighttime or in the early morning. From the analysis of momentum balance, it is apparent that inertial oscillation at nighttime and vertical mixing in the boundary layer during the day are important for diurnal variations. However, diurnal

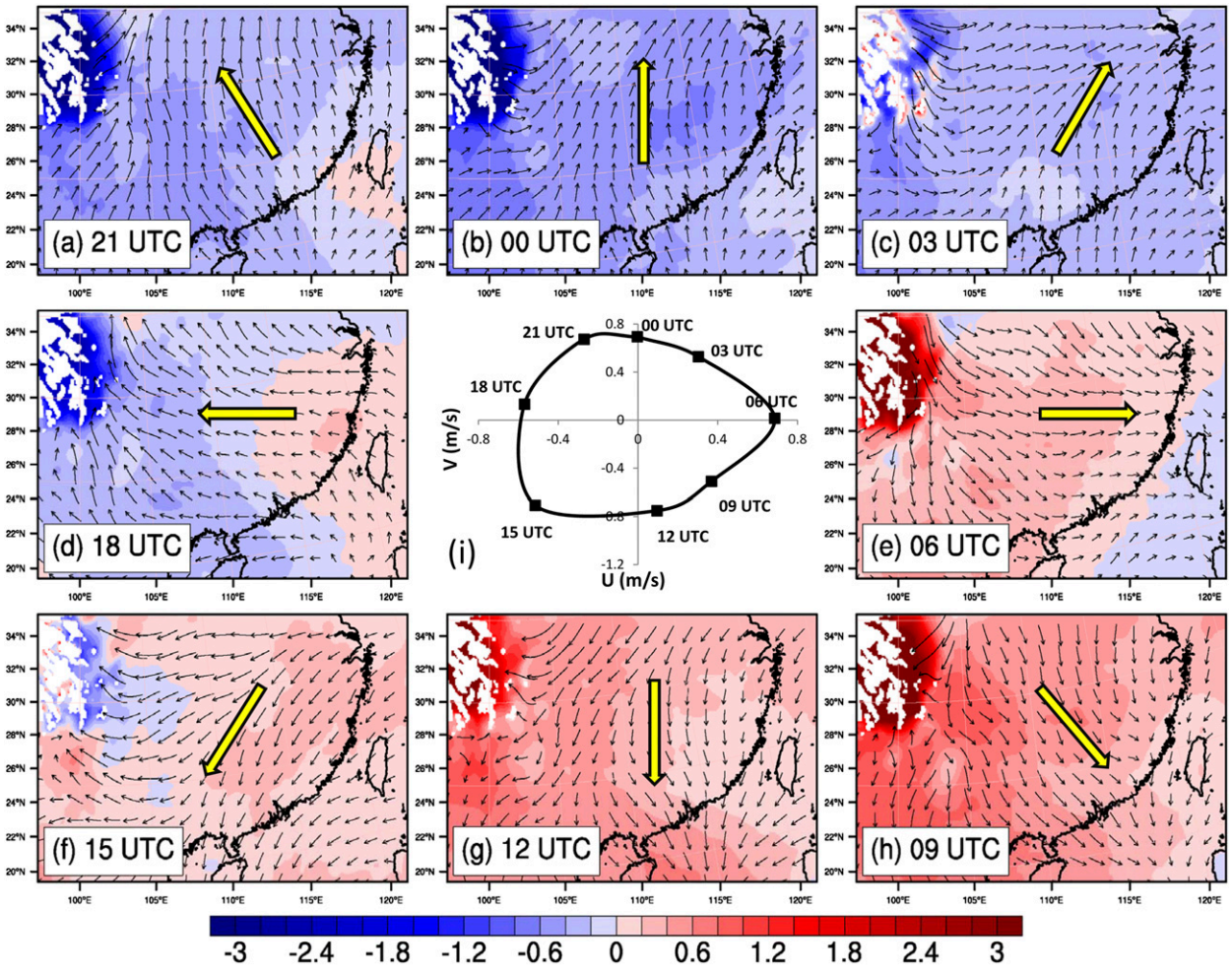

FIG. 19. (a)–(h) Spatial distribution of the 600-hPa perturbation potential temperature (K, colors) and perturbation wind vectors at 0000, 0300, 0600, 0900, 1200, 1500, 1800, and 2100 UTC averaged over July 2006–11. Yellow arrows denote the main directions of perturbation wind over southern China. (i) Clockwise rotation of 600-hPa perturbation wind averaged over purple box IV in Fig. 1.

variations of SLLJ occurrence vary depending on the location. The SLLJs over northeastern China show weak diurnal variations. The SLLJs over southern China, however, have two diurnal modes—propagation and stationary—and seasonal variations. The timing of the maximum diurnal SLLJ occurrence east of TP propagates eastward to 112°E (May), 109°E (June), and 105°E (July), which is generally coincident with diurnal variations of precipitation and vertical motions in upper levels. The horizontal advection term in the momentum equation is the dominant term for the diurnal variations of SLLJs over the diurnal propagation mode area (SB). The diurnal stationary mode of SLLJ is located over the South China Plain (east of propagation mode), especially after the onset of the summer monsoon. The diurnal peak of SLLJs of the stationary mode (1100–1400 LST) leads that of precipitation (1400–1700 LST) by a few hours. From momentum and thermal analysis, the Coriolis force acting on the ageostrophic wind (term III) is a dominant term in the momentum equations, and the inertial oscillation mechanism in the presence of land–sea thermal contrast is the main reason for the diurnal variation of SLLJs over the SCP (stationary mode).

This is the first study to document the spatial distributions of BLJs and SLLJs in China and their diurnal variations in detail using our model data. Further modeling studies with sensitive tests (e.g., turning off surface fluxes or reducing model terrain) or idealized simulations (e.g., Sun and Zhang 2012) may provide additional insights into the impacts of terrain and land surface forcing on the occurrences and diurnal variations of BLJs and SLLJs in different regions of China. The detailed relationship between precipitation and SLLJs over southern China (east of TP) also deserves further study using sensitive tests and idealized simulations.

Acknowledgments. This study is supported by the Chinese 973 program 2013CB430104 and the Chinese National Science Foundation under Grants 40921160380 and 41330421. The authors gratefully acknowledge financial support from the China Scholarship Council.

REFERENCES

Akiyama, T., 1973: The large-scale aspects of the characteristic features of the Baiu front. *Pap. Meteor. Geophys.,* **24,** 157–188.

Bao, X., F. Zhang, and J. Sun, 2011: Diurnal variations of warm-season precipitation east of the Tibetan Plateau over China. *Mon. Wea. Rev.,* **139,** 2790–2810, doi:10.1175/MWR-D-11-00006.1.

Blackadar, A. K., 1957: Boundary layer wind maxima and their significance for the growth of nocturnal inversions. *Bull. Amer. Meteor. Soc.,* **38,** 283–290.

Bonner, W. D., 1968: Climatology of the low level jet. *Mon. Wea. Rev.,* **96,** 833–850, doi:10.1175/1520-0493(1968)096<0833:COTLLJ>2.0.CO;2.

Burk, S. D., and W. T. Thompson, 1996: The summertime low-level jet and marine boundary layer structure along the California coast. *Mon. Wea. Rev.,* **124,** 668–686, doi:10.1175/1520-0493(1996)124<0668:TSLLJA>2.0.CO;2.

Chen, G. T.-J., and C.-C. Yu, 1988: Study of low-level jet and extremely heavy rainfall over northern Taiwan in the mei-yu season. *Mon. Wea. Rev.,* **116,** 884–891, doi:10.1175/1520-0493(1988)116<0884:SOLLJA>2.0.CO;2.

——, C.-C. Wang, and D. T.-W. Lin, 2005: Characteristics of low-level jets over northern Taiwan in mei-yu season and their relationship to heavy rain events. *Mon. Wea. Rev.,* **133,** 20–43, doi:10.1175/MWR-2813.1.

Chen, Q., 1982: The instability of the gravity-inertia wave and its relation to low-level jet and heavy rainfall. *J. Meteor. Soc. Japan,* **60,** 1041–1057.

Chen, X. A., and Y.-L. Chen, 1995: Development of low-level jets during TAMEX. *Mon. Wea. Rev.,* **123,** 1695–1719, doi:10.1175/1520-0493(1995)123<1695:DOLLJD>2.0.CO;2.

Chen, Y.-L., X. A. Chen, and Y.-X. Zhang, 1994: A diagnostic study of the low-level jet during TAMEX IOP 5. *Mon. Wea. Rev.,* **122,** 2257–2284, doi:10.1175/1520-0493(1994)122<2257:ADSOTL>2.0.CO;2.

——, ——, S. Chen, and Y.-H. Kuo, 1997: A numerical study of the low-level jet during TAMEX IOP 5. *Mon. Wea. Rev.,* **125,** 2583–2604, doi:10.1175/1520-0493(1997)125<2583:ANSOTL>2.0.CO;2.

Chou, L. C., C.-P. Chang, and R. T. Williams, 1990: A numerical simulation of the mei-yu front and the associated low level jet. *Mon. Wea. Rev.,* **118,** 1408–1428, doi:10.1175/1520-0493(1990)118<1408:ANSOTM>2.0.CO;2.

Davidson, N. E., K. Kurihara, T. Kato, G. Mills, and K. Puri, 1998: Dynamics and prediction of a mesoscale extreme rain event in the baiu front over Kyushu, Japan. *Mon. Wea. Rev.,* **126,** 1608–1629, doi:10.1175/1520-0493(1998)126<1608:DAPOAM>2.0.CO;2.

Douglas, M. W., A. Valdez-Manzanilla, and R. G. Cueto, 1998: Diurnal variation and horizontal extent of the low-level jet over the northern Gulf of California. *Mon. Wea. Rev.,* **126,** 2017–2025, doi:10.1175/1520-0493(1998)126<2017:DVAHEO>2.0.CO;2.

Du, Y., Q. H. Zhang, Y. Ying, and Y. M. Yang, 2012: Characteristics of low-level jets in Shanghai during the 2008–2009 warm seasons as inferred from wind profiler radar data. *J. Meteor. Soc. Japan,* **90,** 891–903, doi:10.2151/jmsj.2012-603.

Duda, J. D., 2011: WRF simulations of mesoscale convective systems at convection-allowing resolutions. M.S. thesis, Dept. of Geological and Atmospheric Sciences, Iowa State University, 115 pp. [Available online at http://lib.dr.iastate.edu/cgi/viewcontent.cgi?article=1161&context=etd.]

He, H., and F. Zhang, 2010: Diurnal variations of warm-season precipitation over northern China. *Mon. Wea. Rev.,* **138,** 1017–1025, doi:10.1175/2010MWR3356.1.

Holton, J. R., 1967: The diurnal boundary layer wind oscillation above sloping terrain. *Tellus,* **19A,** 199–205, doi:10.1111/j.2153-3490.1967.tb01473.x.

Jiménez, P. A., J. F. González-Rouco, E. García-Bustamante, J. Navarro, J. P. Montávez, J. V.-G. de Arellano, J. Dudhia, and A. Muñoz-Roldan, 2010: Surface wind regionalization over complex terrain: Evaluation and analysis of a high-resolution WRF simulation. *J. Appl. Meteor. Climatol.,* **49,** 268–287, doi:10.1175/2009JAMC2175.1.

Kato, T., 1998: Numerical simulation of the band-shaped torrential rain observed over southern Kyushu, Japan on 1 August 1993. *J. Meteor. Soc. Japan,* **76,** 97–128.

Liu, H.-B., L.-J. Li, and B. Wang, 2012: Low-level jets over southeast China: The warm season climatology of the summer of 2003. *Atmos. Oceanic Sci. Lett.,* **5,** 394–400.

Lo, J. C.-F., Z.-L. Yang, and R. A. Pielke, 2008: Assessment of three dynamical climate downscaling methods using the Weather Research and Forecasting (WRF) model. *J. Geophys. Res.,* **113,** D09112, doi:10.1029/2007JD009216.

Marengo, J. A., W. R. Soares, C. Saulo, and M. Nicolini, 2004: Climatology of the low-level jet east of the Andes as derived from the NCEP–NCAR reanalyses: Characteristics and temporal variability. *J. Climate,* **17,** 2261–2280, doi:10.1175/1520-0442(2004)017<2261:COTLJE>2.0.CO;2.

Matsumoto, S., K. Ninomiya, and S. Yoshizumi, 1971: Characteristic features of Baiu front associated with heavy rainfall. *J. Meteor. Soc. Japan,* **49,** 267–281.

Mitchell, M. J., R. W. Arritt, and K. Labas, 1995: A climatology of the warm season Great Plains low-level jet using wind profiler observations. *Wea. Forecasting,* **10,** 576–591, doi:10.1175/1520-0434(1995)010<0576:ACOTWS>2.0.CO;2.

Parish, T. R., and L. D. Oolman, 2010: On the role of sloping terrain in the forcing of the Great Plains low-level jet. *J. Atmos. Sci.,* **67,** 2690–2699, doi:10.1175/2010JAS3368.1.

Pham, N. T., K. Nakamura, F. A. Furuzawa, and S. Satoh, 2008: Characteristics of low level jets over Okinawa in the Baiu and post-Baiu seasons revealed by wind profiler observations. *J. Meteor. Soc. Japan,* **86,** 699–717, doi:10.2151/jmsj.86.699.

Rife, D. L., J. O. Pinto, A. J. Monaghan, C. A. Davis, and J. R. Hannan, 2010: Global distribution and characteristics of diurnally varying low-level jets. *J. Climate,* **23,** 5041–5064, doi:10.1175/2010JCLI3514.1.

Song, J., K. Liao, R. L. Coulter, and B. M. Lesht, 2005: Climatology of the low-level jet at the southern Great Plains atmospheric boundary layer experiments site. *J. Appl. Meteor.,* **44,** 1593–1606, doi:10.1175/JAM2294.1.

Stensrud, D. J., 1996: Importance of low-level jets to climate: A review. *J. Climate,* **9,** 1698–1711, doi:10.1175/1520-0442(1996)009<1698:IOLLJT>2.0.CO;2.

Sun, J., and F. Zhang, 2012: Impacts of mountain–plains solenoid on diurnal variations of rainfalls along the mei-yu front over the east China plains. *Mon. Wea. Rev.,* **140,** 379–397, doi:10.1175/MWR-D-11-00041.1.

Tao, S., and L. Chen, 1987: A review of recent research on the East Asian summer monsoon in China. *Monsoon Meteorology,* C.-P. Chang and T. N. Krishnamurti, Eds., Oxford University Press, 60–92.

Todd, M. C., R. Washington, S. Raghavan, G. Lizcano, and P. Knippertz, 2008: Regional model simulations of the Bodélé low-level jet of northern Chad during the Bodélé Dust Experiment (BoDEx 2005). *J. Climate,* **21,** 995–1012, doi:10.1175/2007JCLI1766.1.

Van de Wiel, B. J. H., A. F. Moene, G. J. Steeneveld, P. Baas, F. C. Bosveld, and A. A. M. Holtslag, 2010: A conceptual view on inertial oscillations and nocturnal low-level jets. *J. Atmos. Sci.,* **67,** 2679–2689, doi:10.1175/2010JAS3289.1.

Vera, C., and Coauthors, 2006: The South American Low-Level Jet Experiment. *Bull. Amer. Meteor. Soc.,* **87,** 63–77, doi:10.1175/BAMS-87-1-63.

Wang, C.-C., G. T.-J. Chen, and R. E. Carbone, 2004: A climatology of warm-season cloud patterns over East Asia based on GMS infrared brightness temperature observations. *Mon. Wea. Rev.,* **132,** 1606–1629, doi:10.1175/1520-0493(2004)132<1606:ACOWCP>2.0.CO;2.

Wang, D., Y. Zhang, and A. Huang, 2013: Climatic features of the south-westerly low-level jet over southeast China and its association with precipitation over east China. *Asia-Pac. J. Atmos. Sci.,* **49,** 259–270, doi:10.1007/s13143-013-0025-y.

Whiteman, C. D., X. Bian, and S. Zhong, 1997: Low-level jet climatology from enhanced rawinsonde observations at a site in the southern Great Plains. *J. Appl. Meteor.,* **36,** 1363–1376, doi:10.1175/1520-0450(1997)036<1363:LLJCFE>2.0.CO;2.

Xu, W., and E. J. Zipser, 2011: Diurnal variations of precipitation, deep convection and lightning over and east of the eastern Tibetan Plateau. *J. Climate,* **24,** 448–465, doi:10.1175/2010JCLI3719.1.

Yu, X., and T.-Y. Lee, 2010: Role of convective parameterization in simulations of a convection band at grey-zone resolutions. *Tellus,* **62A,** 617–632, doi:10.1111/j.1600-0870.2010.00470.x.

Žagar, N., M. Žagar, J. Cedilnik, G. Gregorič, and J. Rakovec, 2006: Validation of mesoscale low-level winds obtained by dynamical downscaling of ERA40 over complex terrain. *Tellus,* **58A,** 445–455, doi:10.1111/j.1600-0870.2006.00186.x.

Zhang, C. X., Q. H. Zhang, Y. Q. Wang, and X. D. Liang, 2008: Climatology of warm season cold vortices in East Asia: 1979–2005. *Meteor. Atmos. Phys.,* **100,** 291–301, doi:10.1007/s00703-008-0310-y.

Zhang, J. P., and Coauthors, 2012: The impact of circulation patterns on regional transport pathways and air quality over Beijing and its surroundings. *Atmos. Chem. Phys.,* **12,** 5031–5053, doi:10.5194/acp-12-5031-2012.

Zhang, L. X., and Z. C. Li, 2009: A summary of research on cold vortex over northeast China (in Chinese). *Climatic Environ. Res.,* **14,** 218–228.

Zhang, Q. H., K. H. Lau, H. Q. Wang, and S. J. Chen, 2000: Numerical simulation on mesoscale convective system along Mei-Yu front in southern China. *Chin. Sci. Bull.,* **45,** 2093–2096, doi:10.1007/BF03183534.

——, ——, Y. H. Kuo, and S. J. Chen, 2003: A numerical study of a mesoscale convective system over the Taiwan Strait. *Mon. Wea. Rev.,* **131,** 1150–1170, doi:10.1175/1520-0493(2003)131<1150:ANSOAM>2.0.CO;2.